



Subaru High- z Exploration of Low-luminosity Quasars (SHELLQs). XIII. Large-scale Feedback and Star Formation in a Low-luminosity Quasar at $z = 7.07$ on the Local Black Hole to Host Mass Relation

Takuma Izumi^{1,2,27} , Yoshiki Matsuoka³ , Seiji Fujimoto^{4,5} , Masafusa Onoue⁶ , Michael A. Strauss⁷ , Hideki Umehata⁸ , Masatoshi Imanishi^{1,2} , Kotaro Kohno^{9,10} , Toshihiro Kawaguchi¹¹ , Taiki Kawamuro¹² , Shunsuke Baba¹ , Tohru Nagao³ , Yoshiki Toba^{3,13,14} , Kohei Inayoshi¹⁵ , John D. Silverman^{16,17} , Akio K. Inoue^{18,19} , Soh Ikarashi²⁰ , Kazushi Iwasawa²¹ , Nobunari Kashikawa¹⁷ , Takuya Hashimoto²² , Kouichiro Nakanishi^{1,2} , Yoshihiro Ueda¹³ , Malte Schramm²³ , Chien-Hsiu Lee²⁴ , and Hyewon Suh^{25,26}

¹ National Astronomical Observatory of Japan, 2-21-1 Osawa, Mitaka, Tokyo 181-8588, Japan; takuma.izumi@nao.ac.jp

² Department of Astronomical Science, The Graduate University for Advanced Studies, SOKENDAI, 2-21-1 Osawa, Mitaka, Tokyo 181-8588, Japan

³ Research Center for Space and Cosmic Evolution, Ehime University, 2-5 Bunkyo-cho, Matsuyama, Ehime 790-8577, Japan

⁴ Cosmic Dawn Center (DAWN), Copenhagen, Denmark

⁵ Niels Bohr Institute, University of Copenhagen, Jagtvej 128, D-2200 Copenhagen N, Germany

⁶ Max-Planck-Institut für Astronomie, Königstuhl 17, D-69117 Heidelberg, Germany

⁷ Princeton University Observatory, Peyton Hall, Princeton, NJ 08544, USA

⁸ RIKEN Cluster for Pioneering Research, 2-1 Hirosawa, Wako, Saitama 351-0198, Japan

⁹ Institute of Astronomy, Graduate School of Science, The University of Tokyo, 2-21-1 Osawa, Mitaka, Tokyo 181-0015, Japan

¹⁰ Research Center for the Early Universe, Graduate School of Science, The University of Tokyo, 7-3-1 Hongo, Bunkyo-ku, Tokyo 113-0033, Japan

¹¹ Department of Economics, Management and Information Science, Onomichi City University, Hisayamada 1600-2, Onomichi, Hiroshima 722-8506, Japan

¹² Núcleo de Astronomía de la Facultad de Ingeniería, Universidad Diego Portales, Av. Ejército Libertador 441, Santiago, Chile

¹³ Department of Astronomy, Kyoto University, Kitashirakawa-Oiwake-cho, Sakyo-ku, Kyoto 606-8502, Japan

¹⁴ Academia Sinica Institute of Astronomy and Astrophysics, 11F of Astronomy-Mathematics Building, AS/NTU, No.1, Section 4, Roosevelt Road, Taipei 10617, Taiwan

¹⁵ Kavli Institute for Astronomy and Astrophysics, Peking University, Beijing 100871, People's Republic of China

¹⁶ Kavli Institute for the Physics and Mathematics of the Universe (Kavli-IPMU, WPI), The University of Tokyo Institutes for Advanced Study, The University of Tokyo, 5-1-5 Kashiwanoha, Kashiwa, Chiba 277-8583, Japan

¹⁷ Department of Astronomy, School of Science, The University of Tokyo, 7-3-1 Hongo, Bunkyo-ku, Tokyo 113-0033, Japan

¹⁸ Department of Physics, School of Advanced Science and Engineering, Faculty of Science and Engineering, Waseda University, 3-4-1, Okubo, Shinjuku, Tokyo 169-8555, Japan

¹⁹ Waseda Research Institute for Science and Engineering, Faculty of Science and Engineering, Waseda University, 3-4-1, Okubo, Shinjuku, Tokyo 169-8555, Japan

²⁰ Centre for Extragalactic Astronomy, Department of Physics, Durham University, South Road, Durham DH1 3LE, UK

²¹ ICREA and Institut de Ciències del Cosmos, Universitat de Barcelona, IEEC-UB, Martí i Franquès, 1, E-08028 Barcelona, Spain

²² Tomonaga Center for the History of the Universe (TCHoU), Faculty of Pure and Applied Sciences, University of Tsukuba, Tsukuba, Ibaraki 305-8571, Japan

²³ Graduate School of Science and Engineering, Saitama University, 255 Shimo-Okubo, Sakura-ku, Saitama City, Saitama 338-8570, Japan

²⁴ NSF's National Optical-Infrared Astronomy Research Laboratory, 950 North Cherry Avenue, Tucson, AZ 85719, USA

²⁵ Subaru Telescope, National Astronomical Observatory of Japan (NAOJ), 650 North A'ohoku Place, Hilo, HI 96720, USA

²⁶ Gemini Observatory/NSF's NOIRLab, 670 North A'ohoku Place, Hilo, HI 96720, USA

Received 2021 February 26; revised 2021 March 31; accepted 2021 April 10; published 2021 June 14

Abstract

We present Atacama Large Millimeter/submillimeter Array [C II] 158 μm line and underlying far-infrared (FIR) continuum emission observations ($0''.70 \times 0''.56$ resolution) toward HSC J124353.93+010038.5 (J1243+0100) at $z = 7.07$, the only low-luminosity ($M_{1450} > -25$ mag) quasar currently known at $z > 7$. The FIR continuum is bright (1.52 mJy) and resolved with a total luminosity of $L_{\text{FIR}} = 3.5 \times 10^{12} L_{\odot}$. The spatially extended component is responsible for $\sim 40\%$ of the emission. The area-integrated [C II] spectrum shows a broad wing (FWHM = 997 km s^{-1} , $L_{[\text{C II}]} = 1.2 \times 10^9 L_{\odot}$), as well as a bright core (FWHM = 235 km s^{-1} , $L_{[\text{C II}]} = 1.9 \times 10^9 L_{\odot}$). This wing is the first detection of a galactic-scale quasar-driven outflow (atomic outflow rate $> 447 M_{\odot} \text{ yr}^{-1}$) at $z > 7$. The estimated large mass-loading factor of the total outflow (e.g., $\gtrsim 9$ relative to the [C II]-based star formation rate) suggests that this outflow will soon quench the star formation of the host. The core gas dynamics are governed by rotation, with a rotation curve suggestive of a compact bulge ($\sim 3.3 \times 10^{10} M_{\odot}$), although it is not yet spatially resolved. Finally, we found that J1243+0100 has a black hole mass-to-dynamical mass (and to-bulge mass) ratio of $\sim 0.4\%$ ($\sim 1\%$), consistent with the local value within the uncertainties. Our results therefore suggest that the black hole–host coevolution relation is already in place at $z \sim 7$ for this object.

Unified Astronomy Thesaurus concepts: Quasars (1319); AGN host galaxies (2017); Active galaxies (17); Interstellar medium (847); Submillimeter astronomy (1647); High-redshift galaxies (734); Galaxy evolution (594)

1. Introduction

The mass accretion onto a supermassive black hole (SMBH; with a mass of $M_{\text{BH}} \gtrsim 10^{5-6} M_{\odot}$) is invoked to explain the

enormous luminosity observed as an active galactic nucleus (AGN). In the local universe, SMBHs have been identified at the centers of massive galaxies, and there is a tight correlation between M_{BH} and the properties of the host galaxy, such as bulge mass and stellar velocity dispersion (e.g., Magorrian et al. 1998; Ferrarese & Merritt 2000; Marconi & Hunt 2003;

²⁷ NAOJ Fellow.

Kormendy & Ho 2013; Reines & Volonteri 2015). These relations strongly suggest that the formation and growth of SMBHs and host galaxies are intimately linked, a coevolution of these two components of galaxies. Although the detailed mechanisms by which the correlation arises remain unclear, some theoretical models suggest that strong negative AGN feedback on star formation, which is connected to the merger histories of galaxies, plays a key role in driving the coevolution (Sanders et al. 1988; Silk & Rees 1998; Di Matteo et al. 2005; Hopkins et al. 2006). Detections of galaxy-scale AGN-driven outflows in multiphase gas (e.g., Nesvadba et al. 2008; Aalto et al. 2012; Greene et al. 2012; Maiolino et al. 2012; Liu et al. 2013; Cicone et al. 2014; Carniani et al. 2016; Toba et al. 2017), a higher AGN fraction in interacting/merging systems (e.g., Ellison et al. 2011; Silverman et al. 2011; Goulding et al. 2018), and the global similarity in star formation and SMBH accretion histories over cosmic time (Madau & Dickinson 2014, for a review) support this view.

As theoretical models, in principle, make specific predictions for the time evolution of galaxy properties, observations of high-redshift SMBHs and their host galaxies play a crucial role in testing and refining our understanding of the coevolution process (Gallerani et al. 2017; Valiante et al. 2017; Inayoshi et al. 2020). Massive quiescent galaxies already exist in significant numbers at $z \sim 2-3$ (e.g., Straatman et al. 2014; Estrada-Carpenter et al. 2020), suggesting that AGN feedback is important at even higher redshifts. Thus, $z > 6$ quasars, seen when the universe was less than a billion years old, are a unique beacon to study SMBH and galaxy formation. To date, more than 200 quasars with rest-frame ultraviolet (UV) magnitude $M_{1450} \lesssim -22$ mag are known at $z > 5.7$ (Inayoshi et al. 2020), most of which were discovered by wide-field optical and near-infrared surveys (e.g., Bañados et al. 2016; Fan et al. 2001, 2003; Jiang et al. 2016; Matsuoka et al. 2016, 2018a, 2018b, 2019a; Willott et al. 2007, 2010). The sample includes eight quasars at $z > 7$ (Mortlock et al. 2011; Bañados et al. 2018; Wang et al. 2018, 2021; Yang et al. 2019, 2020; Matsuoka et al. 2019a, 2019b). They have SMBH masses of $M_{\text{BH}} \sim 10^9 M_{\odot}$, challenging models for the formation and initial growth of SMBHs at high redshift. It is noteworthy that, already at $z > 7$, some quasars show fast nuclear winds, as evidenced by broad absorption line (BAL) features and blueshifted ionized line emission (Wang et al. 2018, 2021; Onoue et al. 2020; Schindler et al. 2020).

Submillimeter/millimeter observations of the rest-frame far-infrared (FIR) continuum and $\text{C}^+ \text{ } ^2P_{3/2} \rightarrow \text{}^2P_{1/2}$ 157.74 μm ([C II] 158 μm ; one of the prime coolants of the cold interstellar medium, ISM) line emission have revealed that high-redshift quasar host galaxies possess copious amounts of cold gas ($\sim 10^{10} M_{\odot}$) and dust ($\sim 10^8 M_{\odot}$), with high star formation rates (SFRs) of $\gtrsim 100-1000 M_{\odot} \text{ yr}^{-1}$ (e.g., Wang et al. 2010, 2013; Venemans et al. 2016, 2017a, 2020). Maiolino et al. (2012) discovered a massive AGN-driven [C II] outflow (with an estimated neutral outflow rate $> 1400 M_{\odot} \text{ yr}^{-1}$) in the $z = 6.42$ quasar J1148+5251 that extends over $r > 10$ kpc (Cicone et al. 2015). However, this remains the only individual $z > 6$ quasar in which [C II] outflow has been seen. Bischetti et al. (2019) stacked [C II] data cubes of 48 quasars at $z > 4.5$ and claimed to detect a broad (FWHM $\sim 1700 \text{ km s}^{-1}$) component, which they interpreted as a modest AGN-driven outflow ($\sim 100 M_{\odot} \text{ yr}^{-1}$) in the average object. However, Novak et al. (2020) did a

similar stacking analysis of 27 $z \gtrsim 6$ quasars and found no evidence for outflows.

High-resolution interferometric observations predominantly performed by the Atacama Large Millimeter/submillimeter Array (ALMA) have allowed studies of cold gas dynamics in quasar host galaxies (Wang et al. 2013; Venemans et al. 2016; Decarli et al. 2018; Pensabene et al. 2020). These studies revealed that $z \gtrsim 6$ optically luminous ($M_{1450} \lesssim -26$ mag) quasars have, on average, $\sim 10\times$ more massive SMBHs than the local coevolution relations for a given velocity dispersion and/or dynamical mass of the host, suggesting that SMBHs were formed significantly earlier than their host galaxies. This result is in tension with hydrodynamic simulations of quasars (e.g., Hopkins et al. 2006; Lupi et al. 2019; Marshall et al. 2020). However, our understanding of $z \gtrsim 6$ quasars has been biased to the most luminous (and presumably most massive) SMBH population (Lauer et al. 2007; Volonteri & Stark 2011; Schulze & Wisotzki 2014). Indeed, ALMA observations of low-luminosity quasars ($M_{1450} \gtrsim -25$ mag) find that their SFRs are lower ($\lesssim 100 M_{\odot} \text{ yr}^{-1}$) and their SMBH-to-host mass ratios are roughly consistent with the local value (Willott et al. 2013, 2015, 2017; Izumi et al. 2018, 2019). Therefore, sensitive observations of lower-luminosity objects, even at $z > 7$, are necessary to gain a less biased picture of early SMBH/galaxy evolution.

1.1. Our Target: J1243+0100

The wide-field optical deep imaging survey data (the Hyper Suprime-Cam Subaru Strategic Program, HSC-SSP; Aihara et al. 2018) obtained with the HSC (Miyazaki et al. 2012, 2018) mounted on the 8.2 m Subaru telescope have yielded a large number of low-luminosity quasars at redshifts above 6. We have established a multiwavelength follow-up consortium for $z \gtrsim 6$ HSC quasars, the Subaru High- z Exploration of Low-Luminosity Quasars (SHELLQs). SHELLQs (e.g., Matsuoka et al. 2016, 2018a, 2018b) has so far discovered > 90 low-luminosity quasars down to $M_{1450} \sim -22$ mag at $z \gtrsim 6$.

Our target in this work, HSC J124353.93+010038.5 (hereafter J1243+0100), is the only low-luminosity quasar known at $z > 7$, discovered by Matsuoka et al. (2019b). Optical-to-near-infrared spectroscopy allowed determination of the redshift ($z_{\text{Mg II}} = 7.07 \pm 0.01$), UV absolute magnitude ($M_{1450} = -24.13 \pm 0.08$ mag), bolometric luminosity ($L_{\text{bol}} = (1.4 \pm 0.1) \times 10^{46} \text{ erg s}^{-1}$), Mg II-based single-epoch black hole mass ($M_{\text{BH}} = (3.3 \pm 2.0) \times 10^8 M_{\odot}$), and the corresponding Eddington ratio ($\lambda_{\text{Edd}} = 0.34 \pm 0.20$). The luminosity of J1243+0100 is an order of magnitude lower than the other $z > 7$ quasars known to date (Mortlock et al. 2011; Bañados et al. 2018; Wang et al. 2018, 2021; Yang et al. 2019, 2020). Its M_{1450} is close to the knee/characteristic magnitude (M_{1450}^*) of the quasar luminosity function (QLF) at $z \sim 6$ (Matsuoka et al. 2018c). Thus, if the QLF does not evolve significantly from $z \sim 7$ to 6, we can regard J1243+0100 as the first example of a representative quasar at $z > 7$. In addition, J1243+0100 has a CIV $\lambda 1549$ emission line blueshifted by -2400 km s^{-1} relative to Mg II $\lambda 2800$, as well as BAL features indicative of fast nuclear outflows.

In this paper, we present ALMA observations of the [C II] 158 μm line and the underlying rest-frame FIR continuum emission of J1243+0100. This is the 13th in a series of publications presenting the results of SHELLQs. Throughout this work, we adopt the concordant lambda cold dark matter (Λ CDM) cosmology with $H_0 = 70 \text{ km s}^{-1} \text{ Mpc}^{-1}$, $\Omega_{\text{M}} = 0.3$, and $\Omega_{\Lambda} = 0.7$. At the redshift of the source ($z = 7.07$), the age

Table 1
Journal of ALMA Observations

Date (UT) (1)	Antenna Number (2)	Baseline (<i>m</i>) (3)	Integration (minutes) (4)	Calibrator		
				Bandpass (5)	Flux (6)	Phase (7)
2019 Oct 16	41	15.1–740.4	38.5	J1058+0133	J1058+0133	J1232–0224
2019 Oct 22	43	15.1–783.5	38.5	J1058+0133	J1058+0133	J1232–0224
2019 Oct 22	43	15.1–783.5	38.5	J1427–4206	J1427–4206	J1232–0224

Note. (1) Our observations were taken in three sessions on the UT dates listed. (2) Number of antennas used in the observation. (3) Minimum and maximum baseline lengths in meters. (4) Net on-source integration time in minutes. (5)–(7) Calibrators used in the observation.

Table 2
Properties of the Host Galaxy of J1243+0100

	Area-integrated [C II] 158 μm Line Emission		
	Single Gaussian	Double Gaussian (Fit to the Spectrum)	
		Core	Wing
$z_{[\text{C II}]}$	7.0749 ± 0.0001	7.0749 ± 0.0001	Fixed to the core
$\text{FWHM}_{[\text{C II}]} (\text{km s}^{-1})$	280 ± 12	235 ± 17	997 ± 227
$S_{[\text{C II}]} \Delta V (\text{Jy km s}^{-1})$	2.11 ± 0.08	1.59 ± 0.17	1.03 ± 0.21
$L_{[\text{C II}]} (10^9 L_{\odot})$	2.52 ± 0.10	1.90 ± 0.20	1.23 ± 0.25
$\text{SFR}_{[\text{C II}]} (M_{\odot} \text{ yr}^{-1})^{\text{a}}$	220 ± 8	165 ± 17	$107 \pm 22^{\text{b}}$
	Continuum Emission ($T_{\text{dust}} = 47 \text{ K}$, $\beta = 1.6$, $\kappa_{\lambda} = 0.77(850 \mu\text{m}/\lambda)^{\beta} \text{ cm}^2 \text{ g}^{-1}$)		
	Total (imfit)	Extended (<i>uv</i> -plot) ^c	Point Source (<i>uv</i> -plot) ^c
$f_{1.3\text{mm}} (\text{mJy})$	1.52 ± 0.03	0.63 ± 0.04	0.85 ± 0.04
$L_{\text{FIR}} (10^{12} L_{\odot})$	3.5 ± 0.1	1.5 ± 0.1	2.0 ± 0.1
$L_{\text{TIR}} (10^{12} L_{\odot})$	5.0 ± 0.1	2.1 ± 0.1	2.8 ± 0.1
$M_{\text{dust}} (10^8 M_{\odot})$	2.5 ± 0.1	1.0 ± 0.1	1.4 ± 0.1
$\text{SFR}_{\text{TIR}} (M_{\odot} \text{ yr}^{-1})$	742 ± 16	$307 \pm 20^{\text{d}}$	$414 \pm 20^{\text{e}}$

Notes.

^a Based on the calibration for local H II/starburst galaxies (De Looze et al. 2014).

^b This $\text{SFR}_{[\text{C II}]}$ is valid only if the broad wing is due to emission from companion galaxies.

^c We decomposed the continuum emission to a spatially extended component and a point source based on the *uv*-plane analysis.

^d The extended component must be powered by star formation, so the inferred rate for this component represents our conservative estimate for SFR_{TIR} .

^e This SFR_{TIR} is appropriate if this emission is due to star formation, but the dust may be heated by the quasar itself.

of the universe is 0.74 Gyr, and an angular size of $1''$ corresponds to 5.2 kpc.

2. ALMA Observations

We observed the redshifted [C II] line and FIR continuum emission of J1243+0100 in ALMA Band 6 ($\lambda_{\text{obs}} = 1.3 \text{ mm}$) on 2019 October 16 and 22 (ID = 2019.1.00074.S; PI: T. Izumi) as a Cycle 7 program. Our observations were conducted in a single pointing with an $\sim 24''$ diameter field of view (FoV) with 41–43 antennas. Three spectral windows (each $\sim 1.875 \text{ GHz}$ wide) were placed on one sideband to maximize the contiguous frequency coverage. We set the phase-tracking center of this pointing to $(\alpha_{\text{ICRS}}, \delta_{\text{ICRS}}) = (12^{\text{h}}43^{\text{m}}53^{\text{s}}.930, +01^{\circ}00'38''.50)$, which corresponds to the optical quasar position tied to the Gaia astrometry. The baseline length ranged from 15.1 to 740.4 or 783.5 m, resulting in a maximum recoverable scale of $\sim 6''$. The objects J1058+0133 and J1427–4206 were observed as flux and bandpass calibrators, and J1232–0224 was monitored to calibrate the complex gain variation. The total on-source time was 115 minutes. Table 1 summarizes these observations.

The data were processed using CASA (McMullin et al. 2007) version 5.6. All images were reconstructed with the `tclean` task

using natural weighting to maximize the sensitivity. For the [C II] cube, we averaged several channels to obtain a velocity resolution of 75 km s^{-1} , which resulted in a 1σ channel sensitivity of $0.10 \text{ mJy beam}^{-1}$ (beam size = $0''.70 \times 0''.56$, P.A. = $-58^{\circ}.4$). Note that we first deconvolved the line cube including the continuum emission down to the 3σ level to determine the line position and identify the channels free of line emission. These line-free channels were integrated to generate a continuum map ($0''.70 \times 0''.56$, P.A. = $-68^{\circ}.1$, $1\sigma = 13.6 \mu\text{Jy beam}^{-1}$), which we subtracted in the *uv*-plane using the task `uvcontsub` (with a first-order polynomial function), before making the line cube. In this paper, we show only statistical errors unless mentioned otherwise. The absolute flux uncertainty is $\sim 10\%$ (ALMA Cycle 7 Proposer’s Guide). We also used the MIRIAD software (Sault et al. 1995) for some of the analyses in this paper.

3. Results

Both the FIR continuum and the [C II] line emission are clearly detected. We detail their properties in the following and summarize the results in Table 2. The derived properties are compared with those of other $z > 6$ quasars in Section 4.

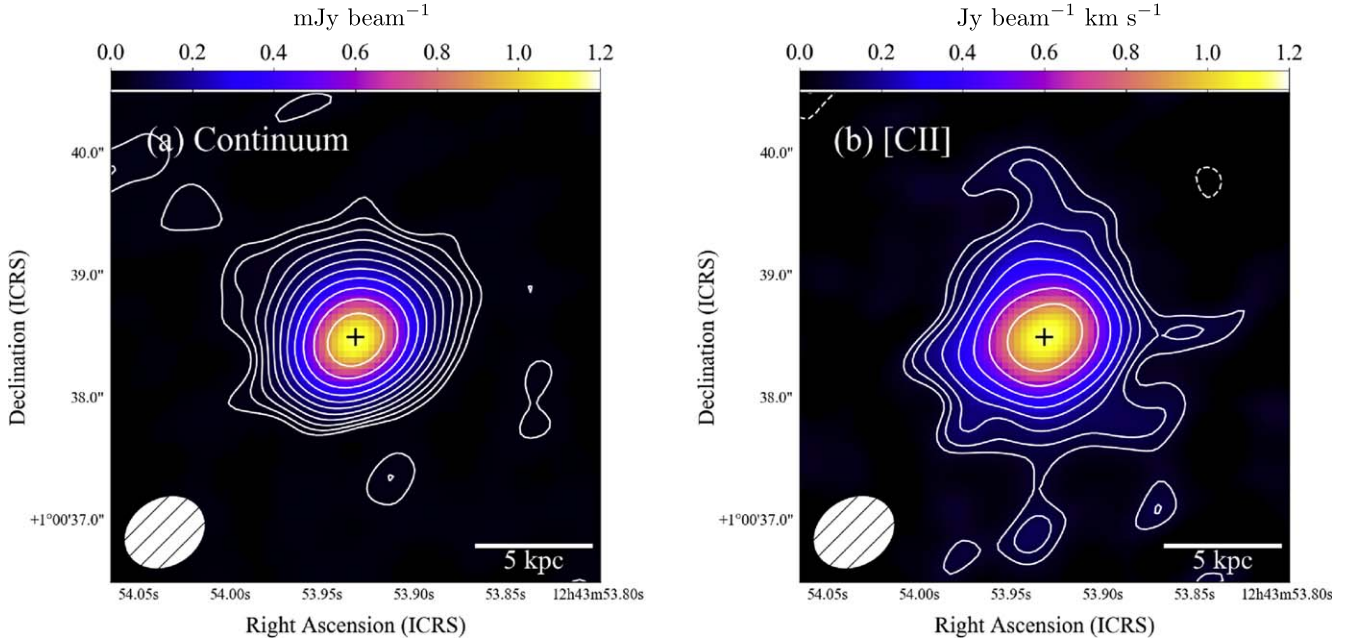


Figure 1. (a) Spatial distribution of the rest-FIR continuum emission of J1243+0100. The image is $4''$ on a side. Contours start at $\pm 2\sigma$ ($1\sigma = 13.6 \mu\text{Jy beam}^{-1}$) and increase by factors of $\sqrt{2}$. (b) Spatial distribution of the velocity-integrated intensity of [C II] $158 \mu\text{m}$. Contours start at $\pm 2\sigma$ ($1\sigma = 0.037 \text{ Jy beam}^{-1} \text{ km s}^{-1}$) and increase by factors of $\sqrt{2}$. In each panel, the synthesized beam is shown in the bottom left corner, and no significant negative emission is found. The central black plus sign denotes the FIR continuum peak position.

3.1. Continuum Properties

Figure 1(a) shows the spatial distribution of the rest-FIR continuum emission. It is very bright, with a peak flux density of $1.15 \text{ mJy beam}^{-1}$ detected at $\sim 85\sigma$ ($1\sigma = 13.6 \mu\text{Jy beam}^{-1}$). This high signal-to-noise ratio (S/N) is well above the threshold of 10 required to make a robust size measurement (Decarli et al. 2018; Venemans et al. 2018). We measured the properties of the source with CASA task `imfit`, which fits a 2D Gaussian to the observed map in the image plane. The emission peaks at $(\alpha_{\text{ICRS}}, \delta_{\text{ICRS}}) = (12^{\text{h}}43^{\text{m}}53^{\text{s}}.932, +01^{\circ}00'38''.49)$, consistent with the optical quasar position (Section 2). Thus, we adopt this FIR continuum peak position as the quasar position. The observed size of the emitting region is $(0''.79 \pm 0''.01) \times (0''.67 \pm 0''.01)$. After deconvolving by the beam, we obtain an intrinsic size of $(0''.38 \pm 0''.03) \times (0''.36 \pm 0''.04)$ or $(2.0 \pm 0.2) \text{ kpc} \times (1.8 \pm 0.2) \text{ kpc}$ at $z = 7.07$ (Table 3). This lies within the range of FIR sizes ($\sim 1\text{--}6 \text{ kpc}$) of previously observed $z \gtrsim 6$ quasars (Izumi et al. 2019; Venemans et al. 2020).

The area-integrated (= total) flux density of this component is $1.52 \pm 0.03 \text{ mJy}$. With this, we first determine the area-integrated FIR luminosity (L_{FIR} ; $42.5\text{--}122.5 \mu\text{m}$) and the total IR luminosity (L_{TIR} ; $8\text{--}1000 \mu\text{m}$) assuming an optically thin modified blackbody spectrum. Following previous studies of $z > 6$ quasars, we assume an intrinsic dust temperature (T_{dust}) of 47 K and a dust spectral emissivity index of $\beta = 1.6$, values that are characteristic of high-redshift optically luminous quasars (Beelen et al. 2006; Leipski et al. 2013). We also correct for the contrast ($\times 1/f_{\text{CMB}}$) and the additional heating effects of the cosmic microwave background (CMB) radiation (da Cunha et al. 2013),

$$f_{\text{CMB}} = 1 - B_{\nu_{\text{rest}}}(T_{\text{CMB},z})/B_{\nu_{\text{rest}}}(T_{\text{dust},z}), \quad (1)$$

$$T_{\text{dust},z} = (T_{\text{dust}}^{4+\beta} + T_{\text{CMB},z=0}^{4+\beta}[(1+z)^{4+\beta} - 1])^{\frac{1}{4+\beta}}, \quad (2)$$

where $T_{\text{CMB},z} = 2.73(1+z) = 22.0 \text{ K}$ at $z = 7.07$, and ν_{rest} is the [C II] rest frequency (1900.54 GHz). With these corrections, we find $L_{\text{FIR}} = (3.5 \pm 0.1) \times 10^{12} L_{\odot}$ and $L_{\text{TIR}} = (5.0 \pm 0.1) \times 10^{12} L_{\odot}$. We also find a dust mass of $M_{\text{dust}} = (2.5 \pm 0.1) \times 10^8 M_{\odot}$ by adopting a rest-frame mass absorption coefficient of $\kappa_{\lambda} = 0.77(850 \mu\text{m}/\lambda)^{\beta} \text{ cm}^2 \text{ g}^{-1}$ (Dunne et al. 2000). Note that these results are sensitive to the assumed values of T_{dust} and β , which are known to be different in different sources (Leipski et al. 2013; Venemans et al. 2018; Liang et al. 2019). For example, varying T_{dust} over the range 35–60 K (e.g., Leipski et al. 2013; Hwang et al. 2010; Dudzevičiūtė et al. 2020) with $\beta = 1.6$ results in $L_{\text{FIR}} = (1.7\text{--}6.1) \times 10^{12} L_{\odot}$. Continuum measurements over a range of wavelengths are needed to constrain T_{dust} . In what follows, we do not include the systematic uncertainty due to the assumed dust temperature.

If we further assume that this IR continuum emission is entirely due to star formation (e.g., Schweitzer et al. 2006; Leipski et al. 2014), we can derive its SFR. We use the conversion $\text{SFR}_{\text{TIR}} = 1.49 \times 10^{-10} L_{\text{TIR}}/L_{\odot}$ (Murphy et al. 2011) and obtain $\text{SFR}_{\text{TIR}} = (742 \pm 16) M_{\odot} \text{ yr}^{-1}$. This conversion is based on the Kroupa initial mass function (IMF; Kroupa 2001) but in accord with other studies (e.g., Kennicutt 1998) after accounting for the differing IMFs assumed therein. If the dust is partially heated by the quasar itself, the true SFR would be lower, so this value is an upper limit (e.g., Symeonidis et al. 2016).

To further explore this possibility, we fit the observed visibilities to a model of an unresolved point source and an extended circular Gaussian (Figure 2). Doing this fit in the uv -plane avoids uncertainties in the deconvolution process (e.g., Ikarashi et al. 2015, 2017; Fujimoto et al. 2019, 2020). Annular averages of the uv data set were created in $20 \text{ k}\lambda$ bins by using the MIRIAD task `uvamp` after shifting the phase center to the exact FIR continuum peak position. The results are

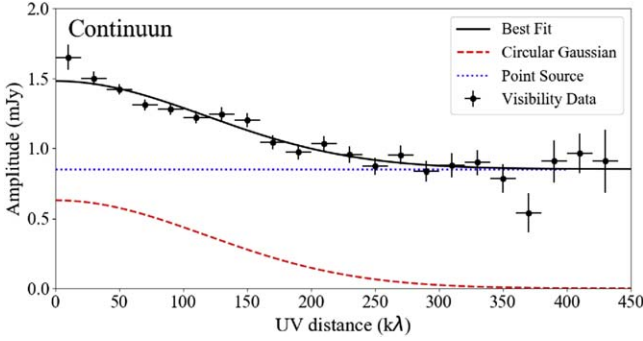


Figure 2. Real part of the continuum visibilities as a function of the uv distance. We modeled this distribution with a combination of a circular Gaussian (FWHM = $0''.66 \pm 0''.06$) and a point-source function. The visibilities are binned in steps of $20 \text{ k}\lambda$.

Table 3
Continuum Spatial Extent (FWHM)

Domain	Size
Image plane (deconvolved)	$(0''.38 \pm 0''.03) \times (0''.36 \pm 0''.04)$ or $(2.0 \pm 0.2) \times (1.8 \pm 0.2) \text{ kpc}^2$
uv -plane	$0''.66 \pm 0''.06$ or $3.4 \pm 0.3 \text{ kpc}$

Note. The uv -plane fit also includes a point-source component (see Figure 2).

summarized in Table 3. The Gaussian component has an FWHM of $0''.66 \pm 0''.06$ ($3.4 \pm 0.3 \text{ kpc}$), likely tracing the star-forming region of this galaxy. The flux density of this component is $0.63 \pm 0.04 \text{ mJy}$, which is equivalent to $\text{SFR}_{\text{TIR}} = 307 \pm 20 M_{\odot} \text{ yr}^{-1}$ ($T_{\text{dust}} = 47 \text{ K}$, $\beta = 1.6$). The point source has a higher flux density ($0.85 \pm 0.04 \text{ mJy}$) than the Gaussian component, resulting in an SFR_{TIR} of $414 \pm 20 M_{\odot} \text{ yr}^{-1}$. However, given that it is unresolved, it may be heated by the quasar itself. Note that Venemans et al. (2018) did not find a significant correlation between L_{Bol} and L_{FIR} (see also Venemans et al. 2020) in optically luminous quasars. On the other hand, Izumi et al. (2021) did find that correlation after expanding the range of L_{Bol} , which may be suggestive of a certain level of quasar contribution to L_{FIR} . Hence, a conservative estimate of $\text{SFR}_{\text{TIR}} (\equiv \text{SFR}_{\text{TIR}}^{\text{CONS}})$ is that obtained from the Gaussian component alone.

3.2. [C II] Line Properties

3.2.1. Global Gas Distribution

Figure 1(b) shows the velocity-integrated [C II] moment-zero map of J1243+0100. We integrate over $\pm 900 \text{ km s}^{-1}$ relative to the systemic redshift given the broad wing component in the area-integrated spectrum (Section 3.2.2). Hence, this choice of the velocity range is the result of an iterative process. Note that, however, the high-velocity component is weak, below 3σ in the (native resolution) velocity channel maps (Figure 3). The [C II] spatial distribution is clearly extended and complex. We applied the CASA task `imfit` to this moment-zero map, which gave a beam-deconvolved size of $(0''.69 \pm 0''.09) \times (0''.67 \pm 0''.10)$ or $(3.6 \pm 0.5) \text{ kpc} \times (3.5 \pm 0.5) \text{ kpc}$. The [C II] flux peak position and the spatial extent are identical within the uncertainties to those of the spatially extended component of

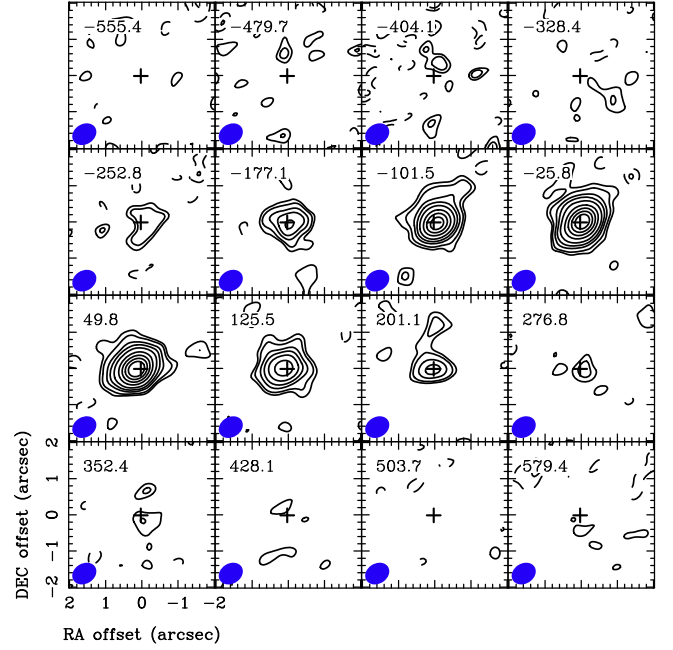


Figure 3. Velocity channel maps of the [C II] line emission of J1243+0100. Each channel is labeled with its central velocity in kilometers per second. The central plus sign in each panel denotes the FIR continuum peak position (Section 3.1). Contours are drawn at -3σ , -2σ , 2σ , 3σ , 5σ , 7σ , 10σ , 15σ , 20σ , 25σ , and 30σ , where $1\sigma = 0.10 \text{ mJy beam}^{-1}$. The synthesized beam is shown in the bottom left corner.

the FIR continuum emission (Table 3). We will perform further detailed size measurements in Section 3.2.4.

3.2.2. Line Spectrum

We extract the [C II] line spectrum (Figure 4) by integrating the signal within the 2σ contours around the center of the moment-zero map. We hereafter refer to this as the area-integrated spectrum. This method gives lower noise than measurement within a circular aperture, particularly when the source is resolved and complex (see detailed discussion in Béthermin et al. 2020). The corresponding 1σ noise level is 0.31 mJy , which was measured from spectral windows above and below the window containing the line emission.

The [C II] spectrum peaks at a flux density of $\sim 7 \text{ mJy}$. This is much brighter than the other HSC quasars observed by ALMA (their peaks are mostly $< 2 \text{ mJy}$; Izumi et al. 2018, 2019). The line spectrum shows a broad component that extends over $\pm 900 \text{ km s}^{-1}$. As we describe in Section 3.2.1, we integrated over this full velocity range to create Figure 1(b) after finding this broad component. Given this broad component, the spectrum is poorly fit with a single Gaussian (Figure 4(a), Table 2) with a returned $\chi^2/\text{d.o.f} = 50.1/27$ (estimated over $\pm 1000 \text{ km s}^{-1}$). A double Gaussian fit (Figure 4(b), Table 2), both centered on the same frequency, gives much better results: $\chi^2/\text{d.o.f} = 16.5/25$. We will discuss the nature of this broad component in Section 4.2.

The narrow core component is likely due to the host galaxy of J1243+0100. The line center redshift is $z_{[\text{C II}]} = 7.0749 \pm 0.0001$. We hereafter regard this as the systemic redshift of this quasar; note that it is consistent with the Mg II–based redshift of 7.07 ± 0.01 (Matsuoka et al. 2019b). With this, we also confirm the large blueshift ($\sim -2400 \text{ km s}^{-1}$) of the C IV emission line (Matsuoka et al. 2019b), indicating the presence

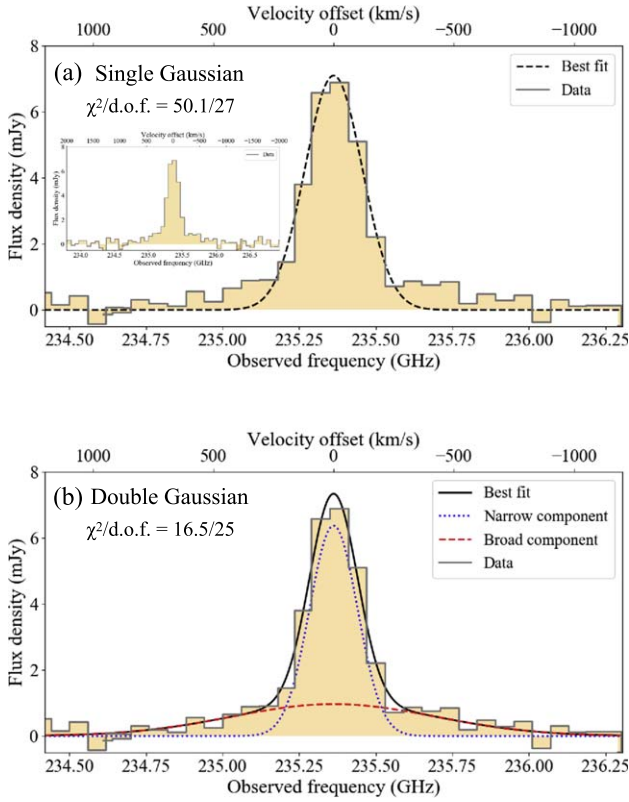


Figure 4. Area-integrated [C II] line spectrum of J1243+0100 measured over a region of [C II] integrated intensity $> 2\sigma \cap r < 2''$. The sensitivity is $0.31 \text{ mJy channel}^{-1}$. Shown are the (a) single and (b) double Gaussian fits to the observed spectrum. The resultant parameters are listed in Table 2. The fit in panel (b) shows a much lower χ^2 than that in panel (a). The inset of panel (a) shows a wider-frequency view, which illustrates the reliability of our continuum subtraction.

of a fast quasar wind. The line width ($\text{FWHM}^{\text{core}} = 235 \pm 17 \text{ km s}^{-1}$) is on the small end of the values found for $z > 6$ quasars of all luminosities (e.g., Decarli et al. 2018; Izumi et al. 2019). As we describe in Section 3.2.4, this is likely due to rotation of a disk at a small inclination angle. The [C II] line luminosity of this component, following Solomon & Vanden Bout (2005), is $L_{[\text{C II}]}^{\text{core}} = (1.90 \pm 0.20) \times 10^9 L_{\odot}$.

By further assuming that the [C II] line is excited primarily by star formation, we can estimate the SFR using the De Looze et al. (2014) calibration based on local H II/starburst galaxies: $\log(\text{SFR}_{[\text{C II}]} / M_{\odot} \text{ yr}^{-1}) = -7.06 + 1.0 \times \log(L_{[\text{C II}]} / L_{\odot})$, with a factor of 2 calibration uncertainty. We obtain $\text{SFR}_{[\text{C II}]}^{\text{core}} = 165 \pm 17 M_{\odot} \text{ yr}^{-1}$, which is consistent within the calibration uncertainty with the result we found from the spatially extended continuum component $\text{SFR}_{\text{FIR}}^{\text{cons}}$. This relation is applicable to high-redshift ($z \sim 4\text{--}8$) star-forming galaxies, as recently demonstrated by Schaerer et al. (2020) and Le Fèvre et al. (2020). If some of the [C II] excitation is in fact due to the quasar, our derived SFR is again an upper limit.

With this core line luminosity and the area-integrated L_{FIR} (i.e., imfit-based value) derived in Section 3.1, we obtain $\log(L_{[\text{C II}]} / L_{\text{FIR}}) = -3.27$. This value is comparable to those of optically luminous $z \gtrsim 6$ quasars (e.g., Wang et al. 2013; Venemans et al. 2016) and $\sim 6\times$ smaller than the canonical Milky Way value ($\sim 3 \times 10^{-3}$; Carilli & Walter 2013). Thus, this quasar follows the so-called [C II]-deficit trend found in ULIRG-class objects (e.g., Malhotra et al. 1997; Stacey et al. 2010; Díaz-Santos et al. 2013) and $z \gtrsim 6$ quasars (e.g.,

Izumi et al. 2019; Venemans et al. 2020). This deficit is likely correlated with a high-FIR surface density (see discussion in, e.g., Decarli et al. 2018; Izumi et al. 2019; Venemans et al. 2020). However, if we use the extended component of the FIR continuum emission (i.e., excluding the point source; Table 3) alone, we obtain $\log(L_{[\text{C II}]} / L_{\text{FIR}}) = -2.89$, which is now close to the Milky Way value. This suggests that the quasar itself contributes to the unresolved component of L_{FIR} , which causes the $L_{[\text{C II}]} / L_{\text{FIR}}$ ratio to be lower in quasars than in starbursts.

We previously emphasized the uncertainty in L_{FIR} due to our lack of knowledge of T_{dust} , which eventually affects our interpretation of $L_{[\text{C II}]} / L_{\text{FIR}}$. To circumvent this issue, we also measure the [C II] equivalent widths. If we use the imfit-based total continuum flux density, we obtain $\text{EW}_{[\text{C II}]} = 0.55 \pm 0.06 \mu\text{m}$, a value only a factor of ~ 2 smaller than the median $\text{EW}_{[\text{C II}]}$ of local starburst galaxies ($\sim 1.0 \mu\text{m}$; Sargsyan et al. 2014). If we instead use the decomposed extended flux density, we find $\text{EW}_{[\text{C II}]} = 1.33 \pm 0.17 \mu\text{m}$, fully consistent with local starbursts. This implies that the ISM physical conditions are not very different between J1243+0100 and the local starbursts. If that is the case, our inferred value of L_{FIR} and the canonical value of $T_{\text{dust}} = 47 \text{ K}$ may be overestimates. However, without multiband FIR data, we will continue to use this canonical dust temperature in what follows.

The broad wing component has $\text{FWHM}^{\text{wing}} = 997 \pm 227 \text{ km s}^{-1}$, with a brightness of $65\% \pm 15\%$ of the core component. The positive and negative velocity wings have identical shapes within the errors, as was seen in the [C II] outflow profile found in J1148+5251 (Maiolino et al. 2012). We will argue in Section 4.2 that these wings are indeed due to cold outflowing gas.

3.2.3. Global Gas Dynamics

We made an intensity-weighted mean velocity map and a velocity dispersion map (Figure 5) using the CASA task `immoments` with a conservative 5σ clipping to avoid noisy pixels. Thus, these maps do not reflect the contribution from the broad wing component. Although the data are convolved with the beam, Figure 5(a) shows a large-scale velocity gradient across the galaxy. This gradient is also apparent in the channel maps (Figure 3) as the peak positions of the [C II] emission move from west to east as a function of channel velocity. We highlight this motion by considering the blue and red sides of the line spectrum; Figure 6 is made by separately integrating the second and third row channels of Figure 3. We found a clear spatial offset of $\sim 0''.2$ (1 kpc) along the east–west direction between the blue and red peaks. Similar velocity gradients over this spatial scale have been observed in some optically luminous quasars (e.g., Wang et al. 2013; Venemans et al. 2016; Shao et al. 2017; Decarli et al. 2018), but some other quasars, including J1342+0928 at $z = 7.54$ and J1120+0641 at $z = 7.09$, are dispersion-dominated systems (Venemans et al. 2017b; Wang et al. 2019; Bañados et al. 2019). The velocity dispersion in Figure 5(b) peaks at $\sim 100 \text{ km s}^{-1}$ at a position slightly offset from the quasar nucleus. Note that beam-smearing and the strong rotation gradient near the nucleus artificially boost the apparent dispersion. Indeed, our dynamical modeling (Section 4.4) suggests that this galaxy is rotation-dominated.

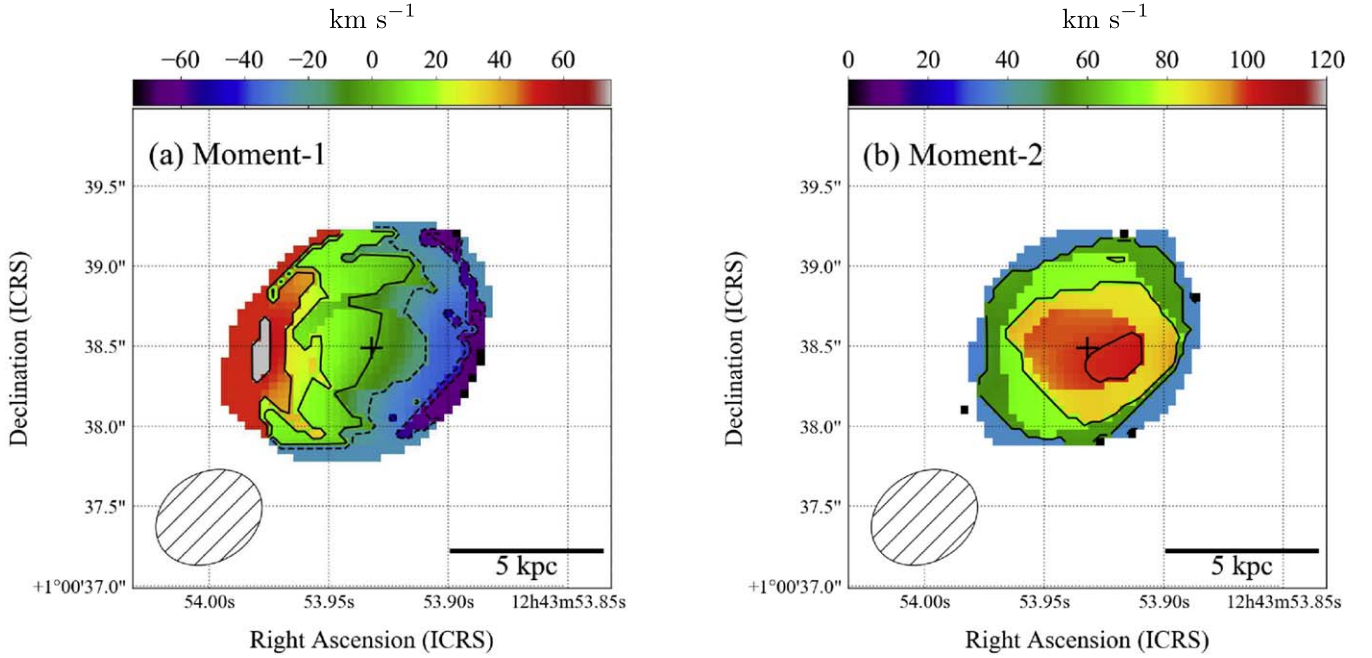


Figure 5. (a) Intensity-weighted [C II] mean velocity map of the central 3'' region of J1243+0100. The contours indicate the velocity relative to the systemic redshift, ranging from -60 to $+60$ km s^{-1} in steps of 20 km s^{-1} . (b) Intensity-weighted velocity dispersion map of the same region. Here the contours indicate 25 , 50 , 75 , and 100 km s^{-1} . These maps were made with a conservative 5σ clipping. In each panel, the bottom left ellipse corresponds to our synthesized beam. The central black plus sign denotes the quasar position.

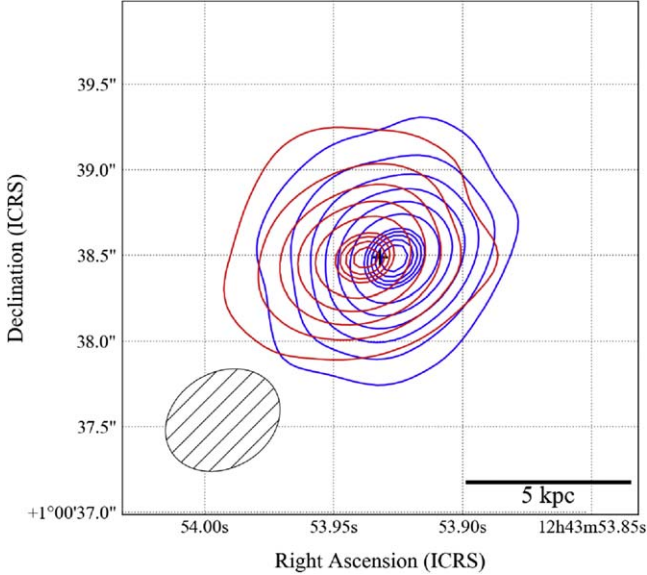


Figure 6. The [C II] intensity distributions integrated over the blue (-253 to -26 km s^{-1} ; blue contours) and red ($+50$ to $+277$ km s^{-1} ; red contours) channels separately. The blue contours indicate 5σ , 10σ , ..., 35σ , 36σ , ..., and 39σ , whereas the red ones indicate 5σ , 10σ , ..., 30σ , 31σ , 32σ , and 33σ , where $1\sigma = 0.015$ $\text{Jy beam}^{-1} \text{km s}^{-1}$. The central plus sign denotes the quasar position.

3.2.4. Decomposed [C II] Spatial Extent

Table 4 lists our measurements of the spatial extent of the narrow core and broad wing components of the [C II] line emission. For this analysis, we regard the core component as the line emission within the 235 km s^{-1} FWHM range determined by our double Gaussian fit (Table 2) and the wing as the line emission outside of that range and within $\pm(250\text{--}900)$ km s^{-1} .

Table 4
[C II] Spatial Extent (FWHM)

Core	
Moment zero (deconvolved)	$(0''.66 \pm 0''.04) \times (0''.58 \pm 0''.03)$ or $(3.4 \pm 0.2) \times (3.0 \pm 0.2)$ kpc^2
Model 1	$0''.81 \pm 0''.04$ or 4.2 ± 0.2 kpc
Wing	
Model 2	$0''.29 \pm 0''.17$ or 1.5 ± 0.9 kpc 3σ limit $< 0''.52$ or < 2.7 kpc

Note. Model N indicates a direct circular Gaussian fit result for the visibilities. In model 1, we fit a single Gaussian function and a point source. In model 2, we only fit a single Gaussian, due to the low S/N of the data in the wing component.

First, we constructed moment-zero maps of these components by separately integrating relevant velocity channels (Figure 7). It is evident that the core component is spatially resolved. While most of the flux lies within $1''$ of the center, there is also a larger ($\sim 2''$) and fainter structure (Figure 7(a)). We first used `imfit` to perform a 2D elliptical Gaussian fit to this image that returned its beam-deconvolved size (FWHM) of $(3.4 \pm 0.2) \times (3.0 \pm 0.2)$ kpc^2 (Table 4). This is consistent with the measured [C II]-emitting region sizes of other $z \gtrsim 6$ quasars (e.g., Decarli et al. 2018; Izumi et al. 2019).

We also modeled the observed visibilities following the analysis in Section 3.1. Figure 8(a) shows the uv -plot of the core component (averaged over the range $235.270\text{--}235.455$ $\text{GHz} = 235$ km s^{-1} FWHM range around the line center). A decline of the visibilities from zero to ~ 200 $\text{k}\lambda$ indicates the existence of an extended (resolved) component, while the contribution from a compact (unresolved) source is apparent at $\gtrsim 250$ $\text{k}\lambda$. The solid line indicates

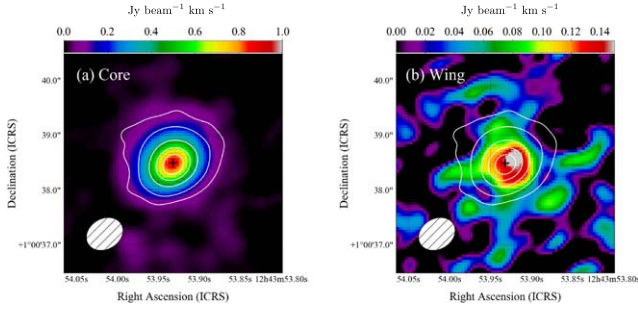


Figure 7. Velocity-integrated [C II] intensity map of the (a) core and (b) wing components. These are made by integrating the -102 to $+126$ km s^{-1} channels for panel (a) and -934 to -253 km s^{-1} plus $+277$ to $+882$ km s^{-1} channels for panel (b) (see also Figures 3 and 4). The central plus sign indicates the quasar location. The contours indicate 3σ , 10σ , 30σ , 50σ , and 70σ of the FIR continuum emission (see also Figure 1a). The 1σ sensitivity is 0.015 and 0.033 $\text{Jy beam}^{-1} \text{km s}^{-1}$ for panels (a) and (b), respectively.

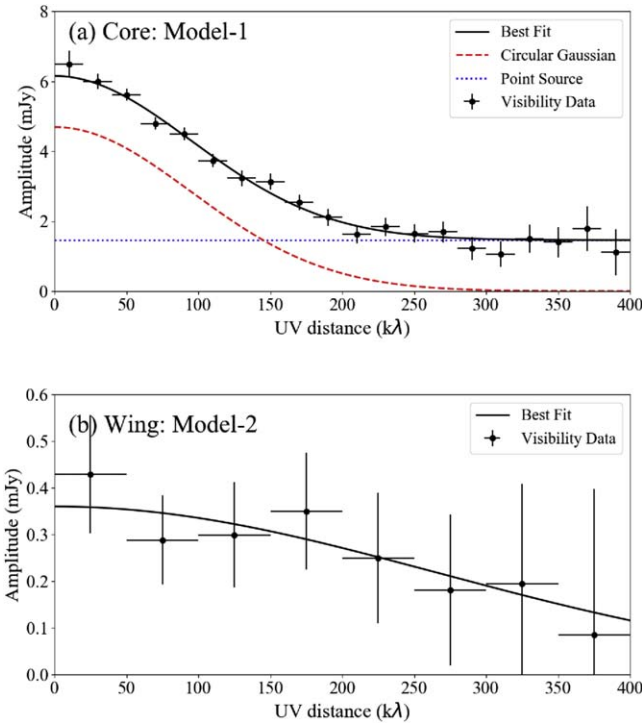


Figure 8. Real part of the [C II] visibilities as a function of the uv distance. (a) Our best-fit model to the core component, consisting of a circular Gaussian ($\text{FWHM} = 0''.81 \pm 0''.04$) and an unresolved point source. (b) Best-fit model for the wing component ($\text{FWHM} = 0''.29 \pm 0''.17$). The extent of the source is less than 3σ from zero. In panel (a), the observed visibilities are binned in steps of 20 $\text{k}\lambda$, whereas in panel (b), we binned in steps of 50 $\text{k}\lambda$ given the faintness of the wing component.

our best-fit model of a point source and a single circular Gaussian distribution (model 1), as has been used in previous works on $z > 6$ quasars (Maiolino et al. 2012; Ciccone et al. 2015). The resultant FWHM ($0''.81 \pm 0''.04$) is $\sim 20\%$ larger than the *imfit* result (Table 4), as we now explicitly model the point source, reducing the central concentration of the Gaussian component.

We also measured the spatial extent of the wing component. While the moment-zero map (Figure 7(b)) is noisy, it suggests that the bulk of the high-velocity flux originates from the central $r < 0''.5$ (i.e., inside the FIR continuum-emitting region). Hence, J1243+0100 itself, rather than companion objects, is likely to be the source of this [C II] wing (Section 4.2). We modeled the visibilities in the wing in 50 $\text{k}\lambda$ bins over the ranges

$234.970\text{--}235.166$ and $235.559\text{--}235.756$ GHz, corresponding to $\pm(250\text{--}500)$ km s^{-1} (bright part of the wing) with a single circular Gaussian fit over <300 $\text{k}\lambda$. We inferred a spatial extent of $\text{FWHM} = 0''.29 \pm 0''.17$ or 1.5 ± 0.9 kpc. This extent is only 1.7σ from zero, so Table 4 also lists the 3σ limit of the extent (2.7 kpc).

3.2.5. Dynamical Mass

With the size of the core component determined from the moment-zero analysis (*imfit*; Table 4) and the line FWHM (Table 2), we can estimate the host galaxy dynamical mass (M_{dyn}). We fit to the data in the image plane, as is standard in $z \gtrsim 6$ quasar studies (e.g., Wang et al. 2013; Willott et al. 2015; Venemans et al. 2016; Izumi et al. 2019). We assume that the line emission originates in a thin rotating disk; the rotation-dominated line-of-sight velocity distribution (Figure 5 and Section 4.4) favors this assumption. The inclination angle of the disk ($i = 20^\circ.5$, where 0° is face-on) is determined from the axis ratio of the deconvolved size. The circular velocity is given by $v_{\text{circ}} = 0.75\text{FWHM} / \sin i$ (i.e., half-width at 20% line maximum). The disk diameter is given by $D = 1.5 \times a_{\text{maj}}$, where a_{maj} is the deconvolved size of the spatial Gaussian major axis, and the factor 1.5 accounts for spatially extended low-level emission (Wang et al. 2013); we indeed see such an extended component (Figures 1 and 7). The M_{dyn} within D is then

$$\left(\frac{M_{\text{dyn}}}{M_{\odot}}\right) = 1.16 \times 10^5 \left(\frac{v_{\text{circ}}}{\text{km s}^{-1}}\right)^2 \left(\frac{D}{\text{kpc}}\right). \quad (3)$$

With the values determined above, we find $M_{\text{dyn}} = (7.6 \pm 0.9) \times 10^{10} M_{\odot}$. The quoted error does not include the uncertainties of the inclination angle or the geometry of the line-emitting region. The inferred dynamical mass is similar to that found for other $z \gtrsim 6$ quasar host galaxies of both high and low nuclear luminosity (e.g., Wang et al. 2013; Willott et al. 2015; Venemans et al. 2016; Izumi et al. 2019). Note that the two other $z > 7$ quasars (J1343+0928 and J1120+0641) observed with ALMA are dispersion-dominated systems with $M_{\text{dyn}} \lesssim (3\text{--}4) \times 10^{10} M_{\odot}$ (Venemans et al. 2017b, 2017c), masses $\gtrsim 2\text{--}3\times$ smaller than we have found for the host galaxy of J1243+0100.

3.3. Continuum Sources in the FoV?

ALMA observations have discovered star-forming companion/merging galaxies to some $z \gtrsim 5$ quasars (e.g., Decarli et al. 2017; Trakhtenbrot et al. 2017; Willott et al. 2017; Neeleman et al. 2019), in accord with the hierarchical galaxy evolution scenario in which quasar activity is driven by mergers (Sanders et al. 1988; Hopkins et al. 2006). We thus searched for companion continuum emitters in our FoV (~ 0.13 arcmin^2) using an S/N map of the region (Figure 9). We found one emission candidate at 4.5σ (i.e., below our 5σ detection threshold), at $(\alpha_{\text{ICRS}}, \delta_{\text{ICRS}}) = (12^{\text{h}}43^{\text{m}}53^{\text{s}}.463, +01^{\circ}00'39''.47)$, which is $7''.1$ (or ~ 37 kpc in projection) from the quasar. No significant line emission is found at this location over our spectral coverage, and no optical counterpart is identified in our HSC maps (g , r , i , z , and y bands). No other source was detected in the field. Given the field number count of sources at 1.2 mm (e.g., Fujimoto et al. 2016), we would predict ~ 1 to

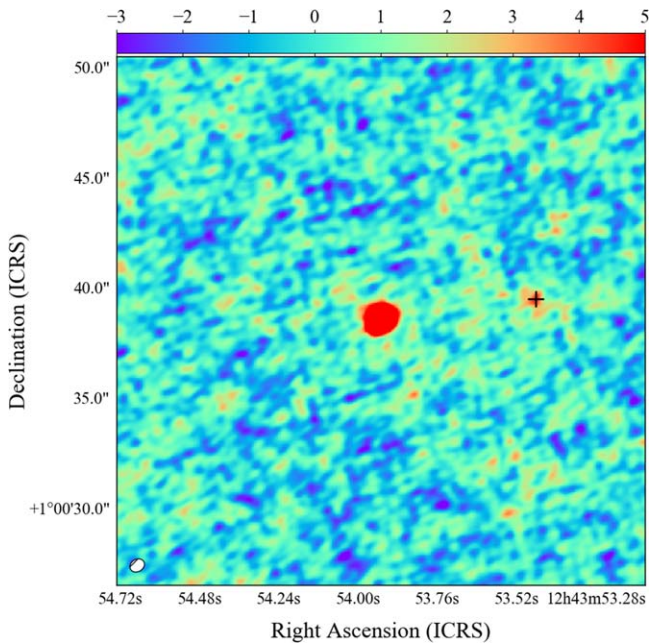


Figure 9. Large-scale S/N map of the rest-FIR continuum emission around J1243+0100. No primary beam correction has been made. Other than the quasar host galaxy itself, no source is detected at $>5\sigma$ ($1\sigma = 13.6 \mu\text{Jy beam}^{-1}$). One apparent object at $4.5''$ (i.e., below our detection threshold) is indicated with a plus sign; it lies $7''1$ (~ 37 kpc) from the quasar in projection. The color scale has units of millijanskys per beam.

three emitters in our FoV; given small number statistics and the cosmic variance, our nondetection is consistent with this result.

Similarly, within the data cube created in Section 2, we did not find any [C II] line emitter²⁸ within our FoV and a velocity range of $\pm 1000 \text{ km s}^{-1}$ relative to the quasar. We will present an analysis using [C II] cubes with different velocity resolutions in a future paper.

4. Discussion

4.1. Comparison of the Star-forming Nature

Under the assumptions made in Section 3, it is intriguing that the SFR_{TIR} of J1243+0100 (including the decomposed conservative value $\text{SFR}_{\text{TIR}}^{\text{cons}}$) is as high as those of $z > 6$ optically luminous quasars (e.g., Venemans et al. 2018, 2020), despite the fact that its quasar nucleus is $>10\times$ fainter than those of the latter. As a reference for future higher-redshift observations, we summarize the observational properties of the currently known $z > 7$ quasars in Table 5.

Seven intrinsically low-luminosity ($M_{1450} > -25$ mag) HSC quasars have been observed with ALMA (Izumi et al. 2018, 2019). Six of them have an inferred SFR_{TIR} a factor of 3–10 lower than that of J1243+0100. The seventh, J2239+0207 at $z = 6.25$, has an FIR luminosity, $L_{\text{FIR}} = 2.2 \times 10^{12} L_{\odot}$, comparable to that of J1243+0100, but it has a close companion galaxy (Izumi et al. 2019), which may have triggered its starburst. Note that another HSC quasar, J1205–0000 ($z = 6.72$), also shows a comparably high L_{FIR} (Izumi et al. 2021), but this source is dust-reddened and indeed as optically luminous as SDSS-class quasars when dust extinction is taken into account (Kato et al. 2020). The luminosity of the

[C II] line (spectral) core component of J1243+0100 is higher than all other HSC quasars (Izumi et al. 2018, 2019), which all have $L_{[\text{C II}]} \leq 1.0 \times 10^9 L_{\odot}$. The quasar VIMOS 2911 (Willott et al. 2017) is the only other optically low-luminosity quasar known at $z > 6$ with an FIR luminosity comparable to J1243+0100. Thus, optically faint but FIR-luminous quasars are a rare population at $z > 6$ –7.

We summarize these findings in Figure 10 in the context of the star-forming main sequence (MS); the majority of normal star-forming galaxies are found to populate a sequence on the galaxy stellar mass M_{\star} –SFR plane (see $z \sim 1$ –2 studies in, e.g., Daddi et al. 2007; Noeske et al. 2007). Galaxies lying above (below) this MS are considered to be starburst (quiescent) systems. The evolution of the MS over cosmic time has been extensively studied up to $z \sim 5$ –6 (e.g., Speagle et al. 2014; Steinhardt et al. 2014; Salmon et al. 2015). While the MS is not well constrained at $z \gtrsim 5$, we compare the SFR of J1243+0100 and other HSC quasars (Izumi et al. 2018, 2019) and optically luminous quasars at $z \gtrsim 6$ (Decarli et al. 2018) with the MS at $z \sim 6$ (Salmon et al. 2015). Here we assume $M_{\text{dyn}} = M_{\star}$, as is frequently done in $z > 6$ quasar studies (e.g., Wang et al. 2013; Willott et al. 2015; Venemans et al. 2016; Pensabene et al. 2020). The dynamical masses of course have large uncertainties and represent an upper limit to the stellar mass. Note that the dynamical masses for the quasars from the literature are computed in the same manner as described in Section 3.2.5.

As observational constraints on the MS at high redshifts $z > 5$ –6 are still limited, we also show the M_{\star} –SFR relation predicted by a semianalytic model, the new numerical galaxy catalog ($\nu^2\text{GC}$; Makiya et al. 2016). In this model, the merging histories of dark matter halos are based on large cosmological N -body simulations (Ishiyama et al. 2015); we adopt the results from the subset of the models with the largest volume ($1.12 h^{-1}$ comoving Gpc box) and the dark matter mass resolution of $2.20 \times 10^8 h^{-1} M_{\odot}$ (8192^3 particles). The model prescriptions for star formation, gas heating and cooling, supernova feedback, SMBH growth, and AGN feedback are described in, e.g., Makiya et al. (2016) and Shirakata et al. (2019). Here we selected $\sim 41,000$ galaxies at $z \sim 6$ that host $M_{\text{BH}} \geq 10^7 M_{\odot}$ SMBHs. The simulation shows both an MS and a starburst sequence; the gap between these two is artificial due to the limited mass and time resolutions of the model (Shirakata et al. 2019).

While in more quasars, the TIR-based SFR lies above the [C II]-based value, the optically luminous quasars of Decarli et al. (2018) are clearly located on or above the MS, whereas the HSC quasars lie on or below the MS. Hence, these two samples populate different regimes in this diagram, likely representing different evolutionary stages. Some HSC quasars seem to be ceasing their star formation already at $z > 6$, and they may evolve into compact and massive quiescent galaxies like those found at $z \sim 3$ –4 (Straatman et al. 2014; Glazebrook et al. 2017; Estrada-Carpenter et al. 2020). In contrast, J1243+0100 is clearly on the starburst sequence based either on SFR_{TIR} or $\text{SFR}_{\text{TIR}}^{\text{cons}}$; it is near the MS if we instead adopt $\text{SFR}_{[\text{C II}]}$. In either case, J1243+0100 is forming stars at a significant rate. This argument is conservative, as M_{dyn} is actually the upper limit of M_{\star} .

One intriguing difference between J1243+0100 and optically luminous $z \gtrsim 6$ –7 quasars would be their Eddington ratios (λ_{Edd}). A large fraction of $z \gtrsim 6$ –7 quasars have λ_{Edd} close to 1 (e.g., Onoue et al. 2019), while $\lambda_{\text{Edd}} = 0.34 \pm 0.20$

²⁸ We define a line emitter as an object with a peak line flux density of $>5\sigma$ and at least two contiguous velocity channels with $>3\sigma$ emission.

Table 5
Properties of $z > 7$ Quasars Known to Date

Object	Redshift	M_{1450} (mag)	M_{BH} (M_{\odot})	$L_{\text{Bol}}/L_{\text{Edd}}$	SFR_{TIR} ($M_{\odot} \text{ yr}^{-1}$)	M_{dyn} (M_{\odot})	Ref.
J0313–1806	7.6423 ± 0.0013 ([C II])	-26.13 ± 0.05	$(1.6 \pm 0.4) \times 10^8$	0.67 ± 0.14	225 ± 25	—	1
J1342+0928	7.5413 ± 0.0007 ([C II])	-26.76 ± 0.04	$9.1^{+1.4}_{-1.3} \times 10^8$	1.1 ± 0.2	150 ± 30	$< 3.2 \times 10^{10}$	2, 3, 4, 5
J1007+2115	7.5149 ± 0.0004 ([C II])	-26.66 ± 0.07	$(1.5 \pm 0.2) \times 10^9$	1.1 ± 0.2	700	—	6
J1120+0461	7.0851 ± 0.0005 ([C II])	-26.6 ± 0.1	$(2.4 \pm 0.2) \times 10^9$	0.48 ± 0.04	315 ± 25	$< 4.3 \times 10^{10}$	7, 8, 9
J1243+0100	7.0749 ± 0.0001 ([C II])	-24.13 ± 0.08	$(3.3 \pm 2.0) \times 10^8$	0.34 ± 0.20	307–742	$(7.6 \pm 0.9) \times 10^{10}$	10, 11
J0038–1527	7.021 ± 0.005 (SED)	-27.10 ± 0.08	$(1.33 \pm 0.25) \times 10^9$	1.25 ± 0.19	—	—	12
J0252–0503	7.02 (SED)	-25.77 ± 0.09	—	—	—	—	13
J2356+0017	7.01 (Ly α)	-25.31 ± 0.04	—	—	—	—	14

Note. The literature values of SFR_{TIR} (or L_{TIR}) are computed in the same manner as described in Section 3.1. References: (1) Wang et al. (2021), (2) Bañados et al. (2018), (3) Onoue et al. (2020), (4) Venemans et al. (2017c), (5) Novak et al. (2019), (6) Yang et al. (2020), (7) Mortlock et al. (2011), (8) De Rosa et al. (2014), (9) Venemans et al. (2017b), (10) Matsuoka et al. (2019b), (11) this work, (12) Wang et al. (2018), (13) Yang et al. (2019), (14) Matsuoka et al. (2019a).

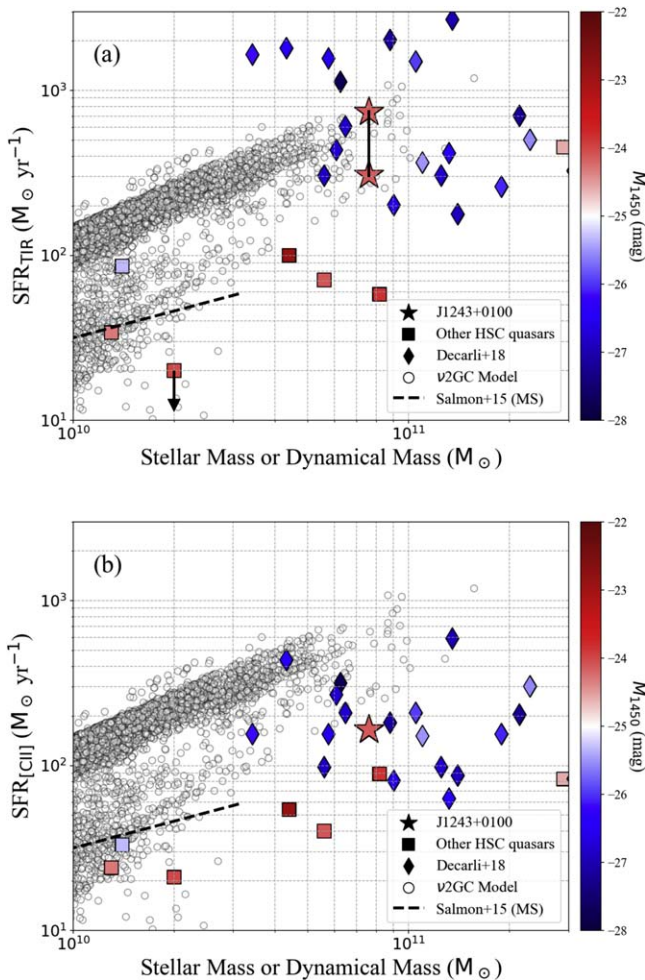


Figure 10. (a) TIR-based and (b) [C II]-based SFRs as a function of M_{dyn} for the HSC quasars (Izumi et al. 2018, 2019) and optically luminous $z \gtrsim 6$ quasars (Decarli et al. 2018). For the SFR_{TIR} of J1243+0100, we plot both the `imfit`-based total value and the `uv-plot`-based decomposed value for the extended component ($\text{SFR}_{\text{TIR}}^{\text{cons}}$). These quasars are color-coded by their M_{1450} . Assuming that $M_{\text{dyn}} = M_*$, we also plot the total SFR and stellar mass for galaxies from the $v^2\text{GC}$ semianalytic model (Shirakata et al. 2019). Two sequences, namely the starburst- and star-forming MSs, are visible in the model. The diagonal dashed line indicates the observed MS suggested from rest-frame UV-to-near-IR photometric observations (Salmon et al. 2015).

(Matsuoka et al. 2019b), a value \sim three times smaller, is found for J1243+0100. Kim & Im (2019) found a similarly high L_{FIR} (or SFR_{TIR}) in some $z \sim 6$ quasars with $\lambda_{\text{Edd}} < 0.2$ and

suggested that feedback was starting to quench the nuclear activity of these objects. We suggest that J1243+0100 is similar. We observe both accretion disk-scale feedback (in the form of BAL winds) and galaxy-scale outflows (Section 4.2). That is, we suggest that J1243+0100 has recently started to clear out the (circum)nuclear gas via feedback, which may soon cause the galaxy-scale star formation to cease (inside-out feedback).

4.2. Nature of the Broad Wing Component

We here discuss the physical origin of the broad [C II] wing seen in Figure 4. It could be due to (a) close companion/merger galaxies or (b) fast [C II] outflows (Izumi et al. 2021). However, we do not consider scenario (a) to be likely for a number of reasons.

1. Companion. No companions are seen in the optical, FIR continuum, or [C II] within $3''$ of the quasar. In the optical, there are no detected companions in our deep Subaru/HSC y -band map with a $5\sigma_{\text{AB}}$ limiting magnitude of 24.65 mag (Matsuoka et al. 2019b).
2. Symmetric line profile. Even if there is a close [C II] companion, its redshift is still (slightly) offset from J1243+0100, which will naturally result in an asymmetric line profile. But the observed broad [C II] wing is almost symmetric, like that seen in the fast [C II] outflow of J1148+5251 (Maiolino et al. 2012). To make this apparent broad symmetric component, we do need multiple companions at a range of velocity offsets within this small region, but would be surprising if the net effect were a symmetric feature. Hence, this scenario would be unlikely.
3. Size of the wing component. The estimated spatial extent of the broad wing is small, $< 0''.52$ (Table 4), and located within the continuum-emitting region (Figure 5). Thus, the mechanism responsible for this broad wing must lie inside this galaxy.
4. Likely rotation-dominated host galaxy. We considered whether violent shocks from a galaxy merger caused this wing. However, this is unlikely; Figure 5(a) shows that the gas motions appear to be dominated by rotation, as we quantify in Section 4.4. A merger, on the other hand, would likely show dispersion-dominant gas dynamics (e.g., Bournaud et al. 2011; Díaz-Santos et al. 2016, 2018; Treister et al. 2020).

We thus conclude that the broad [C II] wing is due to a fast neutral outflow. This is the second individual detection of a [C II] outflow at $z > 6$ after J1148+5251 at $z = 6.4$ (Maiolino et al. 2012; Cicone et al. 2015), and J1243+0100 is now the highest-redshift galaxy yet known with large-scale outflows. Both the peak flux density ratio and the velocity-integrated flux ratio of the broad-to-narrow [C II] components of J1243+0100 are comparable to those of J1148+5251. We now estimate the outflow properties in a similar way to previous analyses (e.g., Maiolino et al. 2012; Bischetti et al. 2019).

First, we define the neutral outflow rate by assuming a constant flow (Lutz et al. 2020) as

$$\dot{M}_{\text{out}} = M_{\text{out}} / \tau_{\text{out}} = M_{\text{out}} v_{\text{out}} / R_{\text{out}}, \quad (4)$$

where M_{out} is the outflowing mass, τ_{out} is the flow timescale, v_{out} is the outflow velocity, and R_{out} is the spatial extent (radius) of the outflow. The wing is symmetric and centered on the [C II] core component (indeed, we forced the two components to have the same center in our fits). We thus adopt $v_{\text{out}} = \text{FWHM}/2$. From the values in Table 2, we find $v_{\text{out}} = 499 \pm 113 \text{ km s}^{-1}$. Here R_{out} is defined as half of the spatial FWHM of the wing component. We use the 3σ upper limit of the wing extent (Table 4), i.e., $R_{\text{out}} < 1.3 \text{ kpc}$, and do not consider its uncertainty for simplicity. This provides a lower limit of \dot{M}_{out} . The outflow mass in neutral hydrogen gas (Hailey-Dunsheath et al. 2010) is computed as

$$\frac{M_{\text{out}}}{M_{\odot}} = 0.77 \left(\frac{0.7 L_{[\text{CII}], \text{broad}}}{L_{\odot}} \right) \left(\frac{1.4 \times 10^{-4}}{X_{\text{C}^+}} \right) \times \frac{1 + 2e^{-91/T_{\text{ex}}} + n_{\text{crit}}/n}{2e^{-91/T_{\text{ex}}}}, \quad (5)$$

where X_{C^+} is the ratio of C^+ abundance to H, T_{ex} is the gas excitation temperature in kelvins, n is the gas volume density in cm^{-3} , and n_{crit} is the critical density of the line, $\sim 3 \times 10^3 \text{ cm}^{-3}$. The factor of 0.7 in the first parenthesis is the typical fraction of [C II] arising from photodissociation regions (PDRs; Hollenbach & Tielens 1997). As we do not know the actual gas density, we compute a lower limit on M_{out} by assuming the high-density limit ($n \gg n_{\text{crit}}$). We also adopt a typical abundance of $X_{\text{C}^+} = 1.4 \times 10^{-4}$ and $T_{\text{ex}} = 200 \text{ K}$ in PDRs (Hollenbach & Tielens 1997) following previous studies of [C II] outflows (e.g., Maiolino et al. 2012; Cicone et al. 2015; Ginolfi et al. 2020). The inferred value of M_{out} is quite insensitive to the assumed value of T_{ex} . Using the measurements in Table 2, we obtain $M_{\text{out}} = (1.2 \pm 0.2) \times 10^9 M_{\odot}$ and $\dot{M}_{\text{out}} > 447 \pm 137 M_{\odot} \text{ yr}^{-1}$, respectively. This \dot{M}_{out} is a strict lower limit because of our treatments of R_{out} and M_{out} .

The above \dot{M}_{out} refers to the neutral atomic component only. However, Fluetsch et al. (2019) observationally studied multiphase outflows in local star-forming galaxies and AGNs and found that a large fraction of the outflowing mass is in the molecular phase (see also Rupke 2018; Veilleux et al. 2005, 2020). Hydrodynamic simulations of a $z = 7.5$ quasar find the same trend, particularly at the central kiloparsec-scale regions (Ni et al. 2018). Based on these results, we estimate that the full outflow rate is roughly a factor of 3 larger than the atomic-only value. This suggests that the total outflow rate for J1243+0100 is $\dot{M}_{\text{out}}^{\text{tot}} \gtrsim 1410 M_{\odot} \text{ yr}^{-1}$.

The estimated $\dot{M}_{\text{out}}^{\text{tot}}$ ($\dot{M}_{\text{out}}^{\text{tot}}$) is $\sim 3 \times$ (or $\sim 9 \times$) larger than the $\text{SFR}_{[\text{C II}]}$ of the spectral core component. This $\dot{M}_{\text{out}}^{\text{tot}}$ ($\dot{M}_{\text{out}}^{\text{tot}}$) is also $\sim 180 \times$ (or $\sim 570 \times$) greater than the mass accretion rate onto the SMBH ($\sim 2.5 M_{\odot} \text{ yr}^{-1}$).²⁹ As these outflow rates are lower limits, the actual mass-loading factors ($\eta \equiv \dot{M}_{\text{out}}^{\text{tot}}/\text{SFR}$) may be even larger. Observations of star-forming galaxies find that η is typically $\sim 1\text{--}3$ over a wide range of SFR and redshift (e.g., Bolatto et al. 2013; Cicone et al. 2014; García-Burillo et al. 2015; Gallerani et al. 2018; Fluetsch et al. 2019; Ginolfi et al. 2020), while AGNs can reach $\eta > 5$ (e.g., Cicone et al. 2014; Fiore et al. 2017; Fluetsch et al. 2019). Therefore, our estimate of η is consistent with quasar-driven outflows.

This conclusion also holds if we adopt SFR_{TIR} instead of $\text{SFR}_{[\text{C II}]}$ (Table 2), as our \dot{M}_{out} is merely a lower limit. For instance, if we consider a moderate-density PDR with $n = 10^3 \text{ cm}^{-3}$, we can already achieve $\eta = \dot{M}_{\text{out}}^{\text{tot}}/\text{SFR}_{\text{TIR}} \sim 5$. Furthermore, if we focus on the spatially extended decomposed FIR continuum (i.e., use the conservative value of $\text{SFR}_{\text{TIR}}^{\text{cons}}$), we find a high $\eta > 5$ for the high-density limit and $\eta \sim 12$ for the case of $n = 10^3 \text{ cm}^{-3}$, for example. It is also rare for starburst-driven neutral outflows to reach velocities greater than $\sim 500\text{--}600 \text{ km s}^{-1}$ even for ULIRG-class objects (e.g., Martin 2005; Rupke et al. 2005; Gallerani et al. 2018; Ginolfi et al. 2020), whereas the observed [C II] profile of J1243+0100 extends to $\sim 900 \text{ km s}^{-1}$. Thus, we conclude that the fast [C II] outflow of J1243+0100 is quasar-driven.

As we pointed out above, this is only the second $z > 6$ quasar known with a [C II] outflow out of dozens of objects observed at submillimeter. This may suggest that such outflows have a small duty cycle, as seen in simulations ($\lesssim 10 \text{ Myr}$; e.g., Costa et al. 2014, 2018a; Zubovas 2018). Very large-scale (extended) outflows, such as the $\sim 30 \text{ kpc}$ scale flow seen in J1148+5251, may also be resolved out, particularly for the case of high-resolution interferometric observations. Note that the currently known highest-redshift ($z = 7.64$) quasar, J0313–1806 (Wang et al. 2021), for example, shows a smaller SFR than J1243+0100, while its quasar nucleus is significantly brighter (Table 5). As J0313–1806 also hosts nuclear fast winds, it is intriguing to seek a galaxy-scale feedback that might have quenched the star formation of the host at a further earlier epoch. In any case, deep and homogeneous observations toward a large number of quasars, with holding sensitivity to extended emission, are necessary to faithfully study outflows.

4.3. Feedback on the Host Galaxy

In order to assess the impact of the outflow on the host galaxy itself—and, in particular, any quenching of star formation—we calculate the outflow kinetic power,

$$\dot{E}_{\text{out}} = \frac{1}{2} \dot{M}_{\text{out}} v_{\text{out}}^2, \quad (6)$$

and the momentum load normalized by the radiative momentum of the quasar as

$$\dot{P}_{\text{out}}/\dot{P}_{\text{AGN}} = \frac{\dot{M}_{\text{out}} v_{\text{out}}}{L_{\text{Bol}}/c}, \quad (7)$$

using the numbers calculated in Section 4.2 (Table 6). By solely using the lower limits of the neutral outflow, we find

²⁹ We estimated this by using the bolometric luminosity (Section 1.1) and a canonical radiative efficiency of 0.1.

Table 6
Outflow Properties

Quantity	Value
v_{out} (km s ⁻¹)	499 ± 113
R_{out} (kpc)	<1.3
τ_{out} (10 ⁶ yr)	<2.6 ± 0.6
M_{out} (10 ⁹ M _⊙)	>1.2 ± 0.2
\dot{M}_{out} (M _⊙ yr ⁻¹)	>447 ± 137
\dot{E}_{out} (10 ⁴³ erg s ⁻¹)	>3.5 ± 1.6
$\dot{E}_{\text{out}}/L_{\text{Bol}}$	≥0.25%
$\dot{P}_{\text{out}}/(L_{\text{Bol}}/c)$	≥3.0
$\dot{M}_{\text{out}}^{\text{tot}}$ (M _⊙ yr ⁻¹)	≥1410

Note. The above quantities refer to the neutral atomic outflow, except for $\dot{M}_{\text{out}}^{\text{tot}}$, which is estimated using the relation in Fluetsch et al. (2019).

$\dot{E}_{\text{out}}/L_{\text{Bol}} \gtrsim 0.25\%$ and $\dot{P}_{\text{out}}/\dot{P}_{\text{AGN}} \gtrsim 3.0$. Again assuming that the total outflow rate is ~ 0.5 dex higher than the atomic-only value, as well as that all phase outflows have comparable velocities, $\dot{E}_{\text{out}}^{\text{tot}}/L_{\text{Bol}}$ and $\dot{P}_{\text{out}}^{\text{tot}}/\dot{P}_{\text{AGN}}$ approach $\sim 1\%$ and ~ 10 , respectively.

It is intriguing that J1243+0100 hosts fast winds on the scale of the accretion disk, as evidenced by significantly blueshifted CIV emission and Si IV and CIV BALs (Matsuoka et al. 2019b). One class of AGN feedback models indeed relies on a coupling between the nuclear wind and the galaxy-scale ISM (e.g., King 2003; King & Pounds 2015). The existence of both the nuclear winds and the large-scale [C II] outflow is a good match to this class of model. The lower limits of $\dot{E}_{\text{out}}^{\text{tot}}/L_{\text{Bol}}$ and $\dot{P}_{\text{out}}^{\text{tot}}/\dot{P}_{\text{AGN}}$ for J1243+0100 are somewhat smaller than but on the same order as the values expected in the energy-conserving³⁰ coupling mode ($\dot{E}_{\text{out}}^{\text{tot}}/L_{\text{Bol}} \sim 5\%$, $\dot{P}_{\text{out}}^{\text{tot}}/\dot{P}_{\text{AGN}} \sim 20$). Such a flow is sufficiently energetic to quench star formation inside the host galaxy (e.g., Zubovas & King 2012; Costa et al. 2014; King & Pounds 2015).

Another class of feedback models explains the large-scale outflows as winds driven by direct AGN radiation pressure onto dusty clouds (e.g., Murray et al. 2005; Ishibashi & Fabian 2015, 2016; Costa et al. 2018a, 2018b), i.e., without invoking intermediary winds. For example, Costa et al. (2018a) performed hydrodynamic simulations of outflows driven by multiscattered radiation pressure. Their simulation results for, e.g., v_{out} , $\dot{E}_{\text{out}}^{\text{tot}}/L_{\text{Bol}}$, and $\dot{P}_{\text{out}}^{\text{tot}}/\dot{P}_{\text{AGN}}$ are quite consistent with the values we estimated for J1243+0100. The simulation also predicts that (i) this mechanism is efficient when the quasar nucleus is obscured, as radiation pressure requires a dense ISM on which to act, and (ii) radiation pressure-driven wind is short-lived (~ 10 Myr), as that process loses efficiency once the ISM becomes extended and diffuse. In accord with these predictions, the relatively compact size and short timescale of the outflow of J1243+0100 (Table 6) suggest that this quasar feedback has just begun. In a later phase of the evolution of the outflow, the value of $\dot{E}_{\text{out}}^{\text{tot}}/L_{\text{Bol}}$ will drop, as is seen in the extended [C II] outflow of J1148+5251 (Cicone et al. 2015). The Costa et al. (2018a) simulations predict that outflows could be launched only in quasars with $L_{\text{Bol}} > 10^{47}$ erg s⁻¹, an order of magnitude more luminous than J1243+0100. However, as the outflow can clear out the circumnuclear gas that is the fuel for SMBH accretion, the L_{Bol} of J1243+0100 may have been

³⁰ That is, the shocked wind flow preserves its thermal energy.

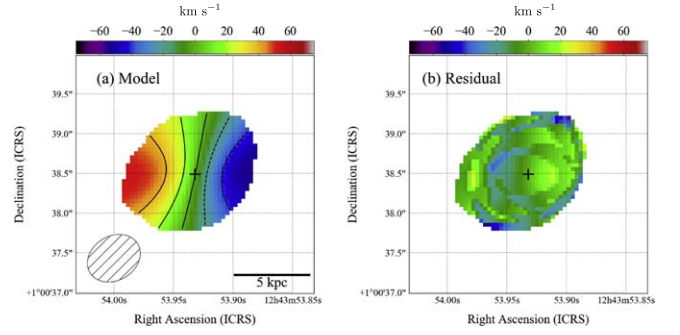


Figure 11. (a) Modeled mean velocity field (moment 1) of J1243+0100. The contours indicate velocities relative to the systemic in steps of ± 20 km s⁻¹. (b) Residual velocity component after subtracting the model from the observed moment-1 map (Figure 5). The residual amplitude is mostly < 20 km s⁻¹, indicating that our fit is good.

much higher at the time the outflow started (e.g., Ciotti et al. 2010; Hopkins & Quataert 2010).

We thus conclude that the outflow properties of J1243+0100 are reasonably consistent with both the energy-conserving wind models and the radiation pressure-driven dusty wind models. Further observational constraints, including outflow geometry, observations of other phases of the outflow, and the stellar and gas mass distributions, may be required for a better comparison with the models. However, we observe a short flow time (Table 6) and ongoing active star formation (Section 4.1), suggesting that no matter what the underlying model, the outflow of J1243+0100 has not yet considerably impacted the star formation of the host galaxy, even though it may already have affected the small-scale gas accretion leading to a relatively small Eddington ratio. Given the high mass-loading factor, this outflow should quench at least the central kiloparsec-scale starburst in the near future.

4.4. Gas Dynamical Modeling

We saw in Section 3.2.3 that the [C II] emission shows what seems to be ordered rotation. In this section, we model the velocity field in detail to extract a rotation curve and velocity dispersion profile. To this end, we fitted six concentric rings with $0''.1$ width to the [C II] data cube using the ^{3D}Barolo code (Di Teodoro & Fraternali 2015), which has been applied to galaxies at both low and high redshift (e.g., Fujimoto et al. 2020; Izumi et al. 2020). The parameters we fit to each ring are V_{rot} , σ_{disp} , and the radial velocity in the disk plane (V_{rad}). We fixed the dynamical center to the quasar position and V_{sys} to 0 km s⁻¹ and constrained the inclination and position angle of the rings to all be the same, with best-fit values of $i = 25^\circ$ and P.A. = 87° , respectively.

A conservative 5σ clipping was applied to avoid noise contamination; hence, our model is not sensitive to the faint outflow. We set initial guesses of $V_{\text{rot}} = 120$, $\sigma_{\text{disp}} = 40$, and $V_{\text{rad}} = 0$ km s⁻¹, respectively, for all rings. The fitting was evaluated by minimizing the residual amplitude, i.e., $|\text{model} - \text{observed data}|$. Figure 11 shows the modeled mean velocity field and the residual map after subtracting the model component from the observed one (Figure 5). The residuals are mostly small, < 20 km s⁻¹ over the modeled regions, indicating the goodness of our fit. We also found that V_{rad} is no larger than ± 20 km s⁻¹; hence, we do not discuss it in further detail hereafter.

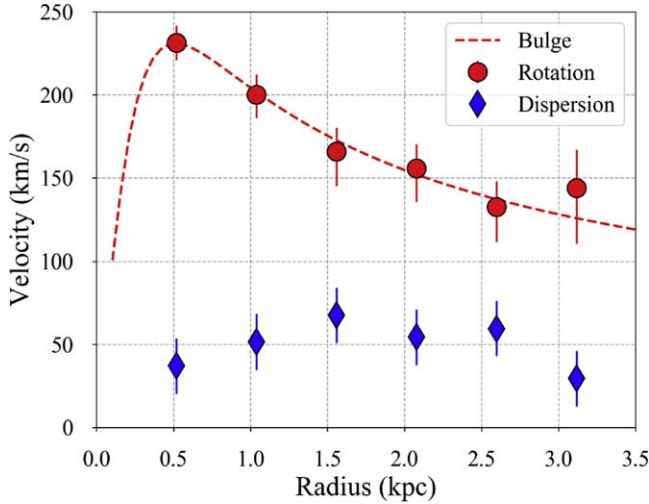


Figure 12. Radial profiles of rotation velocity (V_{rot} ; red circles) and velocity dispersion (σ_{disp} ; blue diamonds) of J1243+0100. The velocities have been corrected for projection due to the inclination of the galaxy. The best-fit Plummer potential (red dashed line) gives a bulge mass of $(3.3 \pm 0.2) \times 10^{10} M_{\odot}$ with a scale length of 0.36 ± 0.03 kpc.

Figure 12 shows the derived V_{rot} and σ_{disp} as a function of radius. The radial velocity is three to five times larger than the velocity dispersion in all bins, clearly indicating that the gas dynamics of J1243+0100 is rotation-dominated. For comparison, the ratio of rotation velocity to velocity dispersion is considerably lower, of order unity, in the well-resolved $z = 6.6$ optically luminous quasar J0305–3150 (Venemans et al. 2019). Models for high-redshift starburst galaxies (without a central AGN) predict a small $V_{\text{rot}}/\sigma_{\text{disp}}$ due to turbulence associated with galaxy mergers, inflows, and stellar feedback (for example, Pillepich et al. 2019 predicted $V_{\text{rot}}/\sigma_{\text{disp}} \lesssim 2$ at $z \sim 5$). Even though $V_{\text{rot}}/\sigma_{\text{disp}}$ is relatively high in J1243+0100, it is not quiescent, given its high SFR (Section 3). Indeed, recent ALMA observations have found rotation-dominated but modestly gravitationally unstable galaxies at $z > 4$ (Tadaki et al. 2018; Rizzo et al. 2020). High-resolution molecular gas observations would allow us to properly assess the gravitational stability of J1243+0100.

It is noteworthy that V_{rot} is highest near the center of the host and drops off in the outer regions. A rotation curve that rises into the central (sub)kiloparsec regions of galaxies is frequently attributed to the existence of a massive galactic bulge (see Sofue 2016, for a review). Indeed, hydrodynamic simulations of $z \gtrsim 7$ quasars found that their host galaxies are typically bulge-dominant massive systems (Tenneti et al. 2019; Marshall et al. 2020). We fit the observed velocity profile $V_{\text{rot}}(r)$ with a simple spherical Plummer potential (Plummer 1911),

$$\Phi(r) = -\frac{GM_{\text{bulge}}}{(r^2 + a^2)^{1/2}}, \quad (8)$$

where G is the gravitational constant and a is the characteristic Plummer radius, which sets the scale length of the core. This simple model fits the observed rotation curve well. The best-fit parameters are $M_{\text{bulge}} = (3.3 \pm 0.2) \times 10^{10} M_{\odot}$ and $a = 0.36 \pm 0.03$ kpc. Given the goodness of the fit, any contributions to the dynamics from other components should be minor at $R \lesssim 3$ kpc. Note that this M_{bulge} is less than half of the M_{dyn} derived in Section 3.2.5. A main cause of this discrepancy may be the crude estimate of the disk circular

velocity for calculating M_{dyn} . Indeed, the estimated v_{circ} in Section 3.2.5 is $\sim 500 \text{ km s}^{-1}$, which is much higher than what we see here in Figure 12. Because of our more detailed modeling in this section, we would think the dynamically modeled M_{bulge} is more robust. Our current data therefore suggest that a massive bulge has already formed in this system at $z \sim 7$. However, our resolution is limited, and thus this estimate of M_{bulge} is tentative. Further higher-resolution and higher-sensitivity observations of gas dynamics with ALMA, as well as direct measurement of the stellar light distribution by the James Webb Space Telescope, will conclusively determine the structure of the host of J1243+0100.

As another aspect, if we crudely assume that the V_{rot} at the scale length ($\sim 220 \text{ km s}^{-1}$) is equivalent to the halo circular velocity, we can roughly estimate the halo mass (M_{h}) by using Equation (25) of Barkana & Loeb (2001). This resulted in $M_{\text{h}} \sim 3 \times 10^{11} M_{\odot}$, which is also consistent with the hydrodynamic simulation result of Marshall et al. (2020) for this class of quasars.

4.5. Early Coevolution at $z \sim 7$

We first treat our measured M_{dyn} (Section 3.2.5) as a surrogate for the bulge-scale stellar mass as usually assumed in $z \gtrsim 6$ quasar studies (e.g., Wang et al. 2013; Venemans et al. 2016; Izumi et al. 2019), allowing us to investigate the black hole–bulge mass relation at this early epoch of the universe. We adopt this simple treatment because detailed rotation curves (and the resultant M_{bulge}) are not currently available in most of the $z > 6$ quasars. Hence, to make a fair comparison with the other $z > 6$ objects, we need to use the crudely estimated M_{dyn} .

Figure 13 shows this relation for $z \gtrsim 6$ quasars using data compiled in Izumi et al. (2019). We computed their M_{dyn} as we did for J1243+0100 in Section 3.2.5. The two $z > 7$ quasars (J1342+0928 and J1120+0641) are dispersion-dominated, and for them, we applied the virial theorem (Venemans et al. 2017b, 2017c; Bañados et al. 2019). The M_{BH} values of all quasars were calculated with the common Vestergaard & Osmer (2009) calibration for the Mg II–based single-epoch method. Some quasars do not have M_{BH} measurements; for them, we assumed Eddington-limited accretion to give the lower mass limits. The low-luminosity objects ($M_{1450} \gtrsim -25$ mag) in this plot were drawn from the HSC sample (Izumi et al. 2018, 2019) and the CFHQS (Willott et al. 2013, 2015, 2017).

It is intriguing that J1243+0100 shows an $M_{\text{BH}}/M_{\text{dyn}}$ ratio in excellent accord with the local value (Kormendy & Ho 2013). It is also in agreement with the cosmological hydrodynamic simulation by Marshall et al. (2020), who predicted an $M_{\text{BH}}-M_{\text{bulge}}$ relation at $z \sim 7$ that is slightly steeper than, but in reasonable agreement with, the local relation (see dotted line in Figure 13). Note, however, that it is possible that gas contributes significantly to M_{dyn} , causing it to be an overestimate of M_{bulge} . Novak et al. (2019) estimated a gas-to-dust mass ratio of the $z = 7.54$ quasar J1342+0928 of < 100 . If we apply this number to the value of M_{dust} of J1243+0100 that we found in Section 3.1, we obtain $M_{\text{gas}} < 2.5 \times 10^{10} M_{\odot}$. Thus, a true (total) stellar mass of this quasar host galaxy would be $\sim (5-7) \times 10^{10} M_{\odot}$, still in good agreement with the expectation from the local relation. Alternatively, if we instead use the direct M_{bulge} estimate of $(3.3 \pm 0.2) \times 10^{10} M_{\odot}$ from Section 4.4, we still find that

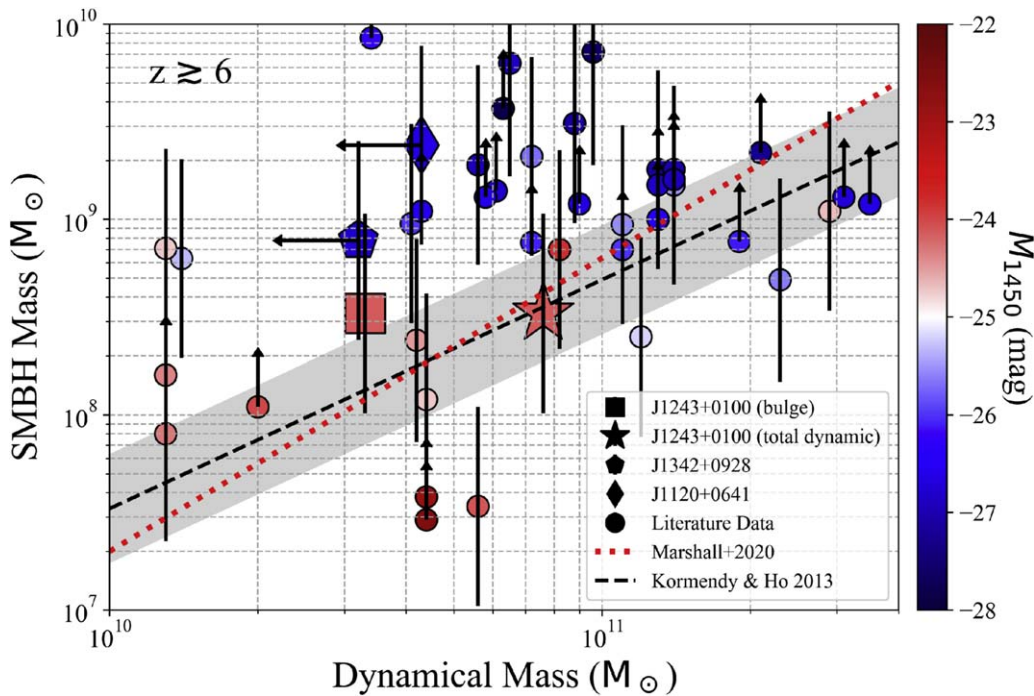


Figure 13. Black hole mass (M_{BH}) vs. host galaxy dynamical mass (M_{dyn}) for $z \gtrsim 6$ quasars, using data compiled from Izumi et al. (2019). The quasars are color-coded by their M_{1450} . Two other $z > 7$ quasars with measured [C II]-based M_{dyn} are highlighted; note that upper limits for their dynamical masses are available. The black dashed line indicates the local $M_{\text{BH}}-M_{\text{bulge}}$ relation (Kormendy & Ho 2013), whereas the red dotted line indicates the simulated relation for $z = 7$ quasars (Marshall et al. 2020).

within the uncertainties, $M_{\text{BH}}/M_{\text{bulge}}$ is consistent with the local value. Our findings therefore suggest that for J1243+0100 at least, the $M_{\text{BH}}-M_{\text{bulge}}$ relation was already in place at $z \sim 7$.

In contrast, the two other $z > 7$ quasars with [C II]-based M_{dyn} estimates (J1342+0928 and J1120+0641) have overmassive black holes relative to these relations by up to a factor of ~ 10 . This is also seen in the other luminous ($M_{1450} \lesssim -26$ mag) quasars at $z \gtrsim 6$, which may reflect a selection bias to more massive black holes (Lauer et al. 2007; Schulze & Wisotzki 2014). Relatively lower-mass SMBHs ($M_{\text{BH}} \lesssim 10^{8.5} M_{\odot}$), most of which are low-luminosity quasars, would not strongly suffer this bias (Lauer et al. 2007; Marshall et al. 2020) and indeed show comparable mass ratios to the local relation (Figure 13). Further observations of galaxies hosting less massive SMBHs are necessary to confirm this picture statistically. As the coevolution relation is the end product of the complex growth of galaxies and SMBHs, a statistical measurement of this relation at the early universe (see also, e.g., Suh et al. 2020; Setoguchi et al. 2021) would help constrain the relative cosmological importance of various feeding and feedback processes (Habouzit et al. 2021). We also need high-resolution observations sensitive to detailed dynamics, as well as wide-area deep observations sensitive to the surrounding environments, to reveal the driving mechanism of the rapid growth of galaxies and SMBHs in the early universe.

5. Summary

In this paper, we present ALMA observations of the [C II] line and underlying rest-frame FIR continuum emission toward J1243+0100 at $z = 7.07$. This object is currently the only low-luminosity quasar known at $z > 7$. We clearly detected both the line and continuum, from which we determined the following characteristics of this remarkable quasar and its host.

1. The FIR continuum is bright, 1.5 mJy, resulting in a total $L_{\text{FIR}} = (3.5 \pm 0.1) \times 10^{12} L_{\odot}$, assuming a dust temperature of $T_{\text{dust}} = 47$ K and an emissivity index of $\beta = 1.6$. The inferred area-integrated SFR_{TIR} is $742 \pm 16 M_{\odot} \text{ yr}^{-1}$ if the heating source is entirely attributed to star formation. We also estimate the dust mass as $(2.5 \pm 0.1) \times 10^8 M_{\odot}$. This inferred SFR is as high as that of optically luminous $z > 6$ quasars and $> 3-10 \times$ higher than that of the low-luminosity HSC quasars observed with ALMA.
2. However, we also decomposed this FIR continuum emission to a point source and an extended Gaussian component. If we regard the former as emission from the quasar nucleus itself, our conservative estimate on SFR_{TIR} should be that of the extended component, i.e., $\text{SFR}_{\text{TIR}}^{\text{cons}} = 307 \pm 20 M_{\odot} \text{ yr}^{-1}$.
3. The [C II] emission is spatially resolved and very bright. We found a broad wing component ($L_{\text{[C II]}} = (1.2 \pm 0.3) \times 10^9 L_{\odot}$, $\text{FWHM} = 997 \pm 227 \text{ km s}^{-1}$) in addition to a bright core component ($L_{\text{[C II]}} = (1.9 \pm 0.2) \times 10^9 L_{\odot}$, $\text{FWHM} = 235 \pm 17 \text{ km s}^{-1}$) in the area-integrated spectrum. The inferred $\text{SFR}_{\text{[C II]}}$ from this spectral core component is $165 \pm 17 M_{\odot} \text{ yr}^{-1}$.
4. We measured the spatial extents of the [C II] spectral core and wing emission by directly modeling the visibilities and found ~ 4.2 kpc for the core and < 2.7 kpc (3σ limit) for the wing. Thus, the broad wing originates from a relatively compact region inside this galaxy.
5. The global gas dynamics is governed by rotation. We estimate its dynamical mass as $M_{\text{dyn}} = (7.6 \pm 0.9) \times 10^{10} M_{\odot}$. This is $\gtrsim 2-3 \times$ larger than the other two $z > 7$ quasars (J1343+0928 and J1120+0641) with M_{dyn} measurements.

6. We did not find any significant ($>5\sigma$) companion continuum emitter within our FoV. This nondetection is, however, consistent with recent 1.2 mm number counts in the field.
7. Using the M_{dyn} as a proxy for the host galaxy stellar mass (M_*), we found that J1243+0100 is located on or even above the star-forming MS at $z \sim 6$. Considering its low quasar luminosity and Eddington ratio, it is plausible that J1243+0100 is in a transition phase; feedback may be in the process of turning off the central quasar activity, but that has not yet shut down the star formation in the host.
8. Various considerations have led us to conclude that the broad [C II] wing is due to a fast neutral outflow, with a rate $\dot{M}_{\text{out}} > 447 \pm 137 M_{\odot} \text{ yr}^{-1}$. Including a molecular component would make this value higher, leading to a high mass-loading factor (e.g., $\gtrsim 9$ relative to $\text{SFR}_{[\text{C II}]}$). This high value suggests that this outflow is quasar-driven. The outflow kinetic power and momentum load are reasonably consistent with the predictions of both the energy-conserving and the radiation pressure-driven wind models. The high mass-loading factor indicates that this outflow will quench the starburst of this galaxy in the near future.
9. By modeling the observed velocity field, we found that the host galaxy dynamics is dominated by rotation, with $V_{\text{rot}}/\sigma_{\text{disp}} \sim 3\text{--}5$. The rotation curve is highest within 1 kpc, which we model as due to a compact (radius ~ 0.36 kpc) stellar bulge with a mass of $(3.3 \pm 0.2) \times 10^{10} M_{\odot}$. While this result is limited by our resolution, we imply that massive bulge formation has already occurred at $z \sim 7$, in accord with the recent model prediction.
10. Using either the (total) dynamical mass or inferred bulge mass from our rotation curve modeling, we find a bulge-to-black hole mass ratio consistent with the local value. Our result therefore suggests that the coevolution relation was already in place at $z \sim 7$.

We have suggested in this paper that a fraction of optically low-luminosity but FIR-luminous quasars are in a key transition phase, ceasing their nuclear activity due to feedback from a powerful outflow. The nuclear fast winds seen in J1243+0100 indicate that this quasar provides an outstanding laboratory to study quasar-driven feedback processes on scales from the accretion disk to the host galaxy. Future ALMA observations will allow us to continue the search for and study of galaxy-scale feedback in these early universe systems.

We appreciate the anonymous reviewer's very constructive comments to improve this manuscript. This paper makes use of the following ALMA data: ADS/JAO.ALMA#2019.1.00074. S. ALMA is a partnership of ESO (representing its member states), NSF (USA) and NINS (Japan), together with NRC (Canada), MOST and ASIAA (Taiwan), and KASI (Republic of Korea), in cooperation with the Republic of Chile. The Joint ALMA Observatory is operated by ESO, AUI/NRAO and NAOJ.

The Hyper Suprime-Cam (HSC) collaboration includes the astronomical communities of Japan and Taiwan and Princeton University. The HSC instrumentation and software were developed by the National Astronomical Observatory of Japan (NAOJ), the Kavli Institute for the Physics and Mathematics of the Universe (Kavli IPMU), the University of Tokyo, the High

Energy Accelerator Research Organization (KEK), the Academia Sinica Institute for Astronomy and Astrophysics in Taiwan (ASIAA), and Princeton University. Funding was contributed by the FIRST program from the Japanese Cabinet Office, the Ministry of Education, Culture, Sports, Science and Technology (MEXT), the Japan Society for the Promotion of Science (JSPS), the Japan Science and Technology Agency (JST), the Toray Science Foundation, NAOJ, Kavli IPMU, KEK, ASIAA, and Princeton University.

T.H. was supported by the Leading Initiative for Excellent Young Researchers, MEXT, Japan (HJH02007). T.I., K.K., A. I., and S.B. were supported by JSPS KAKENHI grant Nos. JP20K14531, JP17H06130, JP17H01114, and JP19J00892, respectively. K.K. and A.I. were also supported by NAOJ ALMA Scientific Research grant Nos. 2017-06B and 2020-16B, respectively. K.I. acknowledges support by the Spanish MICINN under grant PID2019-105510GB-C33 and "Unit of Excellence María de Maeztu 2020-2023" awarded to ICCUB (CEX2019-000918-M). This work is partially supported by the National Science Foundation of China (11721303, 11991052, 11950410493, 12073003) and the National Key R&D Program of China (2016YFA0400702). S.F. acknowledges support from the European Research Council (ERC) Consolidator Grant funding scheme (project ConTEXT, grant No. 648179) and Independent Research Fund Denmark grant DFF-7014-00017. The Cosmic Dawn Center is funded by the Danish National Research Foundation under grant No. 140. T.I. is supported by ALMA Japan Research Grant of the NAOJ ALMA Project, NAOJ-ALMA-253.

ORCID iDs

Takuma Izumi  <https://orcid.org/0000-0001-9452-0813>
 Seiji Fujimoto  <https://orcid.org/0000-0001-7201-5066>
 Masafusa Onoue  <https://orcid.org/0000-0003-2984-6803>
 Michael A. Strauss  <https://orcid.org/0000-0002-0106-7755>
 Hideki Umehata  <https://orcid.org/0000-0003-1937-0573>
 Masatoshi Imanishi  <https://orcid.org/0000-0001-6186-8792>
 Kotaro Kohno  <https://orcid.org/0000-0002-4052-2394>
 Toshihiro Kawaguchi  <https://orcid.org/0000-0002-3866-9645>
 Taiki Kawamuro  <https://orcid.org/0000-0002-6808-2052>
 Shunsuke Baba  <https://orcid.org/0000-0002-9850-6290>
 Tohru Nagao  <https://orcid.org/0000-0002-7402-5441>
 Yoshiki Toba  <https://orcid.org/0000-0002-3531-7863>
 Kohei Inayoshi  <https://orcid.org/0000-0001-9840-4959>
 John D. Silverman  <https://orcid.org/0000-0002-0000-6977>
 Akio K. Inoue  <https://orcid.org/0000-0002-7779-8677>
 Kazushi Iwasawa  <https://orcid.org/0000-0002-4923-3281>
 Nobunari Kashikawa  <https://orcid.org/0000-0003-3954-4219>
 Takuya Hashimoto  <https://orcid.org/0000-0002-0898-4038>
 Kouichiro Nakanishi  <https://orcid.org/0000-0002-6939-0372>
 Yoshihiro Ueda  <https://orcid.org/0000-0001-7821-6715>
 Malte Schramm  <https://orcid.org/0000-0001-7825-0075>
 Chien-Hsiu Lee  <https://orcid.org/0000-0003-1700-5740>
 Hyewon Suh  <https://orcid.org/0000-0002-2536-1633>

References

- Aalto, S., Garcia-Burillo, S., Muller, S., et al. 2012, *A&A*, 537, A44
 Aihara, H., Armstrong, R., Bickerton, S., et al. 2018, *PASJ*, 70, S8
 Bañados, E., Novak, M., Neeleman, M., et al. 2019, *ApJL*, 881, L23

- Bañados, E., Venemans, B. P., Decarli, R., et al. 2016, *ApJS*, 227, 11
- Bañados, E., Venemans, B. P., Mazzucchelli, C., et al. 2018, *Natur*, 553, 473
- Barkana, R., & Loeb, A. 2001, *PhR*, 349, 125
- Beelen, A., Cox, P., Benford, D. J., et al. 2006, *ApJ*, 642, 694
- Béthermin, M., Fudamoto, Y., Ginolfi, M., et al. 2020, *A&A*, 643, A2
- Bischetti, M., Maiolino, R., Carniani, S., et al. 2019, *A&A*, 630, A59
- Bolatto, A. D., Warren, S. R., Leroy, A. K., et al. 2013, *Natur*, 499, 450
- Bournaud, F., Chapon, D., Teyssier, R., et al. 2011, *ApJ*, 730, 4
- Carilli, C. L., & Walter, F. 2013, *ARA&A*, 51, 105
- Carniani, S., Marconi, A., Maiolino, R., et al. 2016, *A&A*, 591, A28
- Cicone, C., Maiolino, R., Gallerani, S., et al. 2015, *A&A*, 574, A14
- Cicone, C., Maiolino, R., Sturm, E., et al. 2014, *A&A*, 562, A21
- Ciotti, L., Ostriker, J. P., & Proga, D. 2010, *ApJ*, 717, 708
- Costa, T., Rosdahl, J., Sijacki, D., & Haehnelt, M. G. 2018a, *MNRAS*, 479, 2079
- Costa, T., Rosdahl, J., Sijacki, D., & Haehnelt, M. G. 2018b, *MNRAS*, 473, A197
- Costa, T., Sijacki, D., & Haehnelt, M. G. 2014, *MNRAS*, 444, 2355
- da Cunha, E., Groves, B., Walter, F., et al. 2013, *ApJ*, 766, 13
- Daddi, E., Dickinson, M., Morrison, G., et al. 2007, *ApJ*, 670, 156
- De Looze, I., Cormier, D., Lebouiteiller, V., et al. 2014, *A&A*, 568, A62
- De Rosa, G., Venemans, B. P., Decarli, R., et al. 2014, *ApJ*, 790, 145
- Decarli, R., Walter, F., Venemans, B. P., et al. 2017, *Natur*, 545, 457
- Decarli, R., Walter, F., Venemans, B. P., et al. 2018, *ApJ*, 854, 97
- Di Matteo, T., Springel, V., & Hernquist, L. 2005, *Natur*, 433, 604
- Di Teodoro, E. M., & Fraternali, F. 2015, *MNRAS*, 451, 3021
- Díaz-Santos, T., Armus, L., Charmandaris, V., et al. 2013, *ApJ*, 774, 68
- Díaz-Santos, T., Assef, R. J., Blain, A. W., et al. 2016, *ApJL*, 816, L6
- Díaz-Santos, T., Assef, R. J., Blain, A. W., et al. 2018, *Sci*, 362, 1034
- Dudzevičiūtė, U., Smail, I., Swinbank, A. M., et al. 2020, *MNRAS*, 494, 3828
- Dunne, L., Eales, S., Edmunds, M., et al. 2000, *MNRAS*, 315, 115
- Ellison, S. L., Patton, D. R., Mendel, J. T., & Scudder, J. M. 2011, *MNRAS*, 418, 2043
- Estrada-Carpenter, V., Papovich, C., Momcheva, I., et al. 2020, *ApJ*, 898, 171
- Fan, X., Narayanan, V. K., Lupton, R. H., et al. 2001, *AJ*, 122, 2833
- Fan, X., Strauss, M. A., Schneider, D. P., et al. 2003, *AJ*, 125, 1649
- Ferrarese, L., & Merritt, D. 2000, *ApJL*, 539, L9
- Fiore, F., Feruglio, C., Shankar, F., et al. 2017, *A&A*, 601, A143
- Fluetsch, A., Maiolino, R., Carniani, S., et al. 2019, *MNRAS*, 483, 4586
- Fujimoto, S., Ouchi, M., Ferrara, A., et al. 2019, *ApJ*, 887, 107
- Fujimoto, S., Ouchi, M., Ono, Y., et al. 2016, *ApJS*, 222, 1
- Fujimoto, S., Silverman, J. D., Béthermin, M., et al. 2020, *ApJ*, 900, 1
- Gallerani, S., Fan, X., Maiolino, R., & Paccucci, F. 2017, *PASA*, 34, e022
- Gallerani, S., Pallottini, A., Feruglio, C., et al. 2018, *MNRAS*, 473, 1909
- García-Burillo, S., Combes, F., Usero, A., et al. 2015, *A&A*, 580, A35
- Ginolfi, M., Jones, G. C., Béthermin, M., et al. 2020, *A&A*, 633, A90
- Glazebrook, K., Schreiber, C., Labbé, I., et al. 2017, *Natur*, 544, 71
- Goulding, A. D., Greene, J. E., Bezanson, R., et al. 2018, *PASJ*, 70, S37
- Greene, J. E., Zakamska, N. L., & Smith, P. S. 2012, *ApJ*, 746, 86
- Habouzit, M., Li, Y., Somerville, R. S., et al. 2021, *MNRAS*, 503, 1940
- Hailey-Dunsheath, S., Nikola, T., Stacey, G. J., et al. 2010, *ApJL*, 714, L162
- Hollenbach, D. J., & Tielens, A. G. M. 1997, *ARA&A*, 35, 179
- Hopkins, P. F., Hernquist, L., Cox, T. J., et al. 2006, *ApJS*, 163, 1
- Hopkins, P. F., & Quataert, E. 2010, *MNRAS*, 407, 1529
- Hwang, H. S., Elbaz, D., Magdis, G., et al. 2010, *MNRAS*, 409, 75
- Ikarashi, S., Ivison, R. J., Caputi, K. I., et al. 2015, *ApJ*, 810, 133
- Ikarashi, S., Ivison, R. J., Caputi, K. I., et al. 2017, *ApJ*, 835, 286
- Inayoshi, K., Visbal, E., & Haiman, Z. 2020, *ARA&A*, 58, 27
- Ishibashi, W., & Fabian, A. C. 2015, *MNRAS*, 451, 93
- Ishibashi, W., & Fabian, A. C. 2016, *MNRAS*, 463, 1291
- Ishiyama, T., Enoki, M., Kobayashi, M. A. R., et al. 2015, *PASJ*, 67, 61
- Izumi, T., Nguyen, D. D., Imanishi, M., et al. 2020, *ApJ*, 898, 75
- Izumi, T., Onoue, M., Matsuoka, Y., et al. 2019, *PASJ*, 71, 111
- Izumi, T., Onoue, M., Matsuoka, Y., et al. 2021, *ApJ*, 908, 235
- Izumi, T., Onoue, M., Shirakata, H., et al. 2018, *PASJ*, 70, 36
- Jiang, L., McGreer, I. D., Fan, X., et al. 2016, *ApJ*, 833, 222
- Kato, N., Matsuoka, Y., Onoue, M., et al. 2020, *PASJ*, 72, 84
- Kennicutt, R. C. J. 1998, *ARA&A*, 36, 189
- Kim, Y., & Im, M. 2019, *ApJ*, 879, 117
- King, A. 2003, *ApJL*, 596, L27
- King, A., & Pounds, K. 2015, *ARA&A*, 53, 115
- Kormendy, J., & Ho, L. C. 2013, *ARA&A*, 51, 511
- Kroupa, P. 2001, *MNRAS*, 322, 231
- Lauer, T. R., Tremaine, S., Richstone, D., & Faber, S. M. 2007, *ApJ*, 670, 249
- Le Fèvre, O., Béthermin, M., Faisst, A., et al. 2020, *A&A*, 643, A1
- Leipski, C., Meisenheimer, K., Walter, F., et al. 2013, *ApJ*, 772, 103
- Leipski, C., Meisenheimer, K., Walter, F., et al. 2014, *ApJ*, 785, 154
- Liang, L., Feldmann, R., Kereš, D., et al. 2019, *MNRAS*, 489, 1397
- Liu, G., Zakamska, N. L., Greene, J. E., Nesvadba, N. P. H., & Liu, X. 2013, *MNRAS*, 436, 2576
- Lupi, A., Volonteri, M., Decarli, R., et al. 2019, *MNRAS*, 488, 4004
- Lutz, D., Sturm, E., Janssen, A., et al. 2020, *A&A*, 633, A134
- Madau, P., & Dickinson, M. 2014, *ARA&A*, 52, 415
- Magorrian, J., Tremaine, S., Richstone, D., et al. 1998, *AJ*, 115, 2285
- Maiolino, R., Gallerani, S., Neri, R., et al. 2012, *MNRAS*, 425, L66
- Makiya, R., Enoki, M., Ishiyama, T., et al. 2016, *PASJ*, 68, 25
- Malhotra, S., Helou, G., Stacey, G., et al. 1997, *ApJL*, 491, L27
- Marconi, A., & Hunt, L. K. 2003, *ApJL*, 589, L21
- Marshall, M. A., Ni, Y., Di Matteo, T., et al. 2020, *MNRAS*, 499, 3819
- Martin, C. L. 2005, *ApJ*, 621, 227
- Matsuoka, Y., Iwasawa, K., Onoue, M., et al. 2018b, *ApJS*, 237, 5
- Matsuoka, Y., Iwasawa, K., Onoue, M., et al. 2019a, *ApJ*, 883, 183
- Matsuoka, Y., Onoue, M., Kashikawa, N., et al. 2016, *ApJ*, 828, 26
- Matsuoka, Y., Onoue, M., Kashikawa, N., et al. 2018a, *PASJ*, 70, S35
- Matsuoka, Y., Onoue, M., Kashikawa, N., et al. 2019b, *ApJL*, 872, L2
- Matsuoka, Y., Strauss, M. A., Kashikawa, N., et al. 2018c, *ApJ*, 869, 150
- McMullin, J. P., Waters, B., Schiebel, D., Young, W., & Golap, K. 2007, in ASP Conf. Ser. 376, *Astronomical Data Analysis Software and Systems XVI*, ed. R. A. Shaw, F. Hill, & D. J. Bell (San Francisco, CA: ASP), 127
- Miyazaki, S., Komiyama, Y., Kawanomoto, S., et al. 2018, *PASJ*, 70, S1
- Miyazaki, S., Komiyama, Y., Nakaya, H., et al. 2012, *Proc. SPIE*, 8446, 84460Z
- Mortlock, D. J., Warren, S. J., Venemans, B. P., et al. 2011, *Natur*, 474, 616
- Murphy, E. J., Condon, J. J., Schinnerer, E., et al. 2011, *ApJ*, 737, 67
- Murray, N., Quataert, E., & Thompson, T. A. 2005, *ApJ*, 618, 569
- Neeleman, M., Bañados, E., Walter, F., et al. 2019, *ApJ*, 882, 10
- Nesvadba, N. P. H., Lehnert, M. D., De Breuck, C., Gilbert, A. M., & van Breugel, W. 2008, *A&A*, 491, 407
- Ni, Y., Di Matteo, T., Feng, Y., Croft, R. A. C., & Tenneti, A. 2018, *MNRAS*, 481, 4877
- Noeske, K. G., Weiner, B. J., Faber, S. M., et al. 2007, *ApJL*, 660, L43
- Novak, M., Bañados, E., Decarli, R., et al. 2019, *ApJ*, 881, 63
- Novak, M., Venemans, B. P., Walter, F., et al. 2020, *ApJ*, 904, 131
- Onoue, M., Bañados, E., Mazzucchelli, C., et al. 2020, *ApJ*, 898, 105
- Onoue, M., Kashikawa, N., Matsuoka, Y., et al. 2019, *ApJ*, 880, 77
- Pensabene, A., Carniani, S., Perna, M., et al. 2020, *A&A*, 637, A84
- Pillepich, A., Nelson, D., Springel, V., et al. 2019, *MNRAS*, 490, 3196
- Plummer, H. C. 1911, *MNRAS*, 71, 460
- Reines, A. E., & Volonteri, M. 2015, *ApJ*, 813, 82
- Rizzo, F., Vegetti, S., Powell, D., et al. 2020, *Natur*, 584, 201
- Rupke, D. 2018, *Galax*, 6, 138
- Rupke, D. S., Veilleux, S., & Sanders, D. B. 2005, *ApJS*, 160, 115
- Salmon, B., Papovich, C., Finkelstein, S. L., et al. 2015, *ApJ*, 799, 183
- Sanders, D. B., Soifer, B. T., Elias, J. H., et al. 1988, *ApJ*, 325, 74
- Sargsyan, L., Samsonyan, A., Lebouiteiller, V., et al. 2014, *ApJ*, 790, 15
- Sault, R. J., Teuben, P. J., & Wright, M. C. H. 1995, in ASP Conf. Ser. 77, *Astronomical Data Analysis Software and Systems IV*, ed. R. A. Shaw, H. E. Payne, & J. J. E. Hayes (San Francisco, CA: ASP), 433
- Schaerer, D., Ginolfi, M., Béthermin, M., et al. 2020, *A&A*, 643, A3
- Schindler, J.-T., Farina, E. P., Bañados, E., et al. 2020, *ApJ*, 905, 51
- Schulze, A., & Wisotzki, L. 2014, *MNRAS*, 438, 3422
- Schweitzer, M., Lutz, D., Sturm, E., et al. 2006, *ApJ*, 649, 79
- Setoguchi, K., Ueda, Y., Toba, Y., & Akiyama, M. 2021, *ApJ*, 909, 188
- Shao, Y., Wang, R., Jones, G. C., et al. 2017, *ApJ*, 845, 138
- Shirakata, H., Okamoto, T., Kawaguchi, T., et al. 2019, *MNRAS*, 482, 4846
- Silk, J., & Rees, M. J. 1998, *A&A*, 331, L1
- Silverman, J. D., Kampeczyk, P., Jahnke, K., et al. 2011, *ApJ*, 743, 2
- Sofue, Y. 2016, *PASJ*, 68, 2
- Solomon, P. M., & Vanden Bout, P. A. 2005, *ARA&A*, 43, 677
- Speagle, J. S., Steinhardt, C. L., Capak, P. L., & Silverman, J. D. 2014, *ApJS*, 214, 15
- Stacey, G. J., Hailey-Dunsheath, S., Ferkinhoff, C., et al. 2010, *ApJ*, 724, 957
- Steinhardt, C. L., Speagle, J. S., Capak, P., et al. 2014, *ApJL*, 791, L25
- Straatman, C. M. S., Labbé, I., Spitler, L. R., et al. 2014, *ApJL*, 783, L14
- Suh, H., Civano, F., Trakhtenbrot, B., et al. 2020, *ApJ*, 889, 32
- Symeonidis, M., Giblin, B. M., Page, M. J., et al. 2016, *MNRAS*, 459, 257
- Tadaki, K., Iono, D., Yun, M. S., et al. 2018, *Natur*, 560, 613
- Tenneti, A., Wilkins, S. M., Di Matteo, T., Croft, R. A. C., & Feng, Y. 2019, *MNRAS*, 483, 1388
- Toba, Y., Bae, H.-J., Nagao, T., et al. 2017, *ApJ*, 850, 140
- Trakhtenbrot, B., Lira, P., Netzer, H., et al. 2017, *ApJ*, 836, 8
- Treister, E., Messias, H., Privon, G. C., et al. 2020, *ApJ*, 890, 149

- Valiante, R., Agarwal, B., Habouzit, M., & Pezzulli, E. 2017, *PASA*, **34**, e031
- Veilleux, S., Cecil, G., & Bland-Hawthorn, J. 2005, *ARA&A*, **43**, 769
- Veilleux, S., Maiolino, R., Bolatto, A. D., & Aalto, S. 2020, *A&ARv*, **28**, 2
- Venemans, B. P., Decarli, R., Walter, F., et al. 2018, *ApJ*, **866**, 159
- Venemans, B. P., Neeleman, M., Walter, F., et al. 2019, *ApJL*, **874**, L30
- Venemans, B. P., Walter, F., Decarli, R., et al. 2017a, *ApJ*, **845**, 154
- Venemans, B. P., Walter, F., Decarli, R., et al. 2017b, *ApJ*, **837**, 146
- Venemans, B. P., Walter, F., Decarli, R., et al. 2017c, *ApJL*, **851**, L8
- Venemans, B. P., Walter, F., Neeleman, M., et al. 2020, *ApJ*, **904**, 130
- Venemans, B. P., Walter, F., Zschaechner, L., et al. 2016, *ApJ*, **816**, 37
- Vestergaard, M., & Osmer, P. S. 2009, *ApJ*, **699**, 800
- Volonteri, M., & Stark, D. P. 2011, *MNRAS*, **417**, 2085
- Wang, F., Wang, R., Fan, X., et al. 2019, *ApJ*, **880**, 2
- Wang, F., Yang, J., Fan, X., et al. 2018, *ApJL*, **869**, L9
- Wang, F., Yang, J., Fan, X., et al. 2021, *ApJL*, **907**, L1
- Wang, R., Carilli, C. L., Neri, R., et al. 2010, *ApJ*, **714**, 699
- Wang, R., Wagg, J., Carilli, C. L., et al. 2013, *ApJ*, **773**, 44
- Willott, C. J., Bergeron, J., & Omont, A. 2015, *ApJ*, **801**, 123
- Willott, C. J., Bergeron, J., & Omont, A. 2017, *ApJ*, **850**, 108
- Willott, C. J., Delorme, P., Omont, A., et al. 2007, *AJ*, **134**, 2435
- Willott, C. J., Delorme, P., Reylé, C., et al. 2010, *AJ*, **139**, 906
- Willott, C. J., Omont, A., & Bergeron, J. 2013, *ApJ*, **770**, 13
- Yang, J., Wang, F., Fan, X., et al. 2019, *AJ*, **157**, 236
- Yang, J., Wang, F., Fan, X., et al. 2020, *ApJL*, **897**, L14
- Zubovas, K. 2018, *MNRAS*, **473**, 3525
- Zubovas, K., & King, A. 2012, *ApJL*, **745**, L34